HCF101 is a novel component of the CIA cytosolic iron-sulfur synthesis pathway in the human pathogen *Toxoplasma gondii*

Eléa A. Renaud[1], Ambre J.M. Maupin[1], Laurence Berry[1], Julie Bals[2], Yann Bordat[1], Vincent Demolombe[2], Valérie Rofidal[2], Florence Vignols[2] and Sébastien Besteiro[1*]

[1]*LPHI, Univ. Montpellier, CNRS, INSERM, France;* [2]*IPSiM, Univ. Montpellier, CNRS, INRAE, Institut Agro, France*

*correspondance : *sebastien.besteiro@inserm.fr*

Abstract

Several key cellular functions depend on proteins harboring an iron-sulfur (Fe-S) cofactor. As these Fe-S proteins localize to several subcellular compartments, they require a dedicated machinery for cofactor assembly. For instance, in plants and algae there are Fe-S cluster synthesis pathways localizing to the cytosol, but also present in the mitochondrion and the in chloroplast, two organelles of endosymbiotic origin. *Toxoplasma gondii* is a plastid-bearing parasitic protist responsible for a pathology affecting humans and other warm-blooded vertebrates. We have characterized the *Toxoplasma* homologue of HCF101, originally identified in plants as a protein transferring Fe-S clusters to photosystem I subunits in the chloroplast. Contrarily to plants, we have shown that HCF101 does not localize to the plastid in parasites, but instead is an important component of the cytosolic Fe-S assembly (CIA) pathway which is vital for *Toxoplasma*. While the CIA pathway is widely conserved in eukaryotes, it is the first time the involvement of HCF101 in this pan-eukaryotic machinery is established. Moreover, as this protein is essential for parasite viability and absent from its mammalian hosts, it constitutes a novel and promising potential drug target.

Introduction

Iron-sulfur (Fe-S) clusters are ancient inorganic cofactors of proteins which are essential in virtually all forms of life [1]. These cofactors are found in a variety of proteins involved in numerous electron transfer and metabolic reactions that support key housekeeping cellular functions like respiration, photosynthesis, DNA repair and replication, protein translation, RNA modifications, but also in regulatory proteins and environmental signals sensors [2,3]. The most common clusters, which in most Fe-S proteins function as electron transfer groups [4], are in the rhombic [2Fe-2S], cubane [4Fe-4S], or more rarely the intermediate [3Fe-4S] configuration. Assembly of these cofactors is a carefully controlled process in order to avoid cellular toxicity arising from the accumulation of free Fe and S, which are highly reactive. Different Fe-S cluster assembly pathways developed early in evolution to synthesize the clusters and can be found in archaea, bacteria, and then evolved to mitochondrial, plastidial and cytosolic iron-sulfur assembly machineries in eukaryotes [5,6]. Thus, eukaryotic Fe-S cluster assembly machineries found in organelles of endosymbiotic origin were inherited from Alphaproteobacteria (the 'iron sulfur cluster', or ISC, pathway in the mitochondrion) and Cyanobacteria (the 'sulfur mobilization', or SUF, pathway in plastids), while a specific machinery ('cytosolic iron-sulfur cluster assembly', or CIA) is used for the biogenesis of cytosolic and nuclear Fe-S proteins.

While the individual components of these Fe-S assembly machineries display some structural diversity, they involve similar biochemical steps [7]. Typically, a cysteine desulfurase will generate sulfur from L-cysteine, scaffold proteins and chaperones will provide a molecular platform allowing the assembly of Fe and S into a cluster, and finally carrier proteins will deliver the cluster to target apoproteins. This happens in a similar fashion but with a specific molecular machinery in the three subcellular compartments in which Fe-S cluster synthesis takes place in eukaryotes, with main difference that the early step of CIA depends on the mitochondrial machinery. In fact, although de novo cluster assembly has been suggested to happen in the cytosol of mammalian cells [8], experimental evidence in a large variety of eukaryotes points to the requirement of mitochondrial ISC components, in particular the Nfs1 cysteine desulfurase, to generate a S precursor that will be translocated to the cytosol [9–11]. In mammals and yeast, P-loop NTPases NUBP1 and NUBP2 are the scaffolds for initial [4Fe-4S] Fe-S cluster assembly in the CIA system [12] and electrons are provided by DRE2, together with TAH18 (ATR3 in plants) [13]. Noticeably, some eukaryotes, like plants, lack a NUBP2 homologue and the scaffolding complex is instead composed of a dimer of NBP35, the NUBP1 homologue [14]. NAR1, a protein containing two [4Fe-4S] clusters, then acts as the Fe-S carrier and associates with the CIA targeting complex (CTC) [15]. The CTC, that will recognize client apoproteins through direct interactions and mediate the insertion of the Fe-S cluster, typically comprises MET18/MMS19 (plant/human nomenclature), CIA1/CIAO1, and AE7/CIAO2B [16].

Toxoplasma gondii is a widespread obligate intracellular parasitic protist belonging to the phylum Apicomplexa. Infection is usually harmless to immunocompetent individuals, but can lead to severe, life-threatening, disease in developing fetuses and immunocompromised individuals [17]. This parasite contains two organelles of endosymbiotic origin: a mitochondrion and a relict plastid called apicoplast, which are both of high metabolic importance [18]. Consequently, like in plants and algae *T. gondii* harbors three distinct Fe-S cluster synthesis pathways: the CIA in the cytosol, ISC in the mitochondrion and SUF in the apicoplast [19,20]. The SUF pathway being essential for the survival of the parasite and absent from its mammalian host, its components and client proteins are particularly attractive as potential drug targets [21], which prompted us to look for Fe-S proteins absent from mammals but present in plant and apicomplexan parasites. Investigating the Fe-S cluster assembly components in

68 protists, which are highly divergent phylogenetically from the canonical yeast or mammalian cell
69 models, can bring interesting insights into the evolution of this molecular machinery [22,23].

70 Here, we report the characterization of the *T. gondii* homologue of the high-chlorophyll-fluorescence
71 101 (HCF101) protein, which is typically a plastid-associated Fe-S transfer protein in the plant
72 *Arabidopsis thaliana* [24,25]. Our work shows that TgHCF101 is essential for parasite viability and we
73 demonstrate for the first time its implication in the eukaryotic CIA pathway.

74

75 **Results**

76 *TgHCF101 is a cytosolic protein*

77 HCF101 is a putative P-loop containing nucleoside triphosphate hydrolase that belongs to the
78 Mrp/NBP35 family (also called ApbC) of dimeric iron-sulfur carrier proteins that are found ubiquitously
79 in all domains of life and thus likely appeared early during evolution [26,27]. Compared with the
80 NBP35, in addition to the nucleotide hydrolase domain HCF101 also contains a N-terminal
81 DUF59/MIP18-family domain [28], as well as a C-terminal domain of unknown function (DUF971). We
82 performed homology searches in the http://www.ToxoDB.org database to retrieve members of the
83 Mrp/NPB35 family encoded by the *T. gondii* genome. Besides TgNBP35, that has an unusual
84 mitochondrial localization in *T. gondii* [20,23], we identified TGGT1_318590 as a potential homologue
85 of HCF101. A broader phylogenetic analysis that included members of the Mrp/NPB35 family from a
86 wide variety of eukaryotes (Table S1), revealed that this putative *T. gondii* homologue clearly
87 segregates with members of the HCF101 group (Fig. 1A). Moreover, its primary sequence analysis
88 confirmed a three domain-organization typical of HCF101 proteins (Fig. 2A), and hence TGGT1_318590
89 may be named TgHCF101.

90 In *A. thaliana*, the *HCF101* mutant was found to be impaired in photosynthesis [29]: interfering with
91 HCF101 function has an impact on the maturation of both photosystem I (PSI) and ferredoxin-
92 thioredoxin reductases, which contain [4Fe-4S] clusters [24,25]. The apicoplast harbored by
93 apicomplexan parasites has lost the ability to perform photosynthesis [30], and some members of the
94 Apicomplexa phylum, like *Cryptosporidium*, have even completely lost the plastid [31] while it has
95 retained a HCF101 homologue (Fig. 1A, Fig. S1). Thus, a function linked to photosystem seems unlikely
96 for apicomplexan parasites. Sequence analysis confirmed that, in contrast to plant homologues,
97 TgHCF101 lacks a predicted N-terminal transit peptide, which is typically needed for plastid import (Fig.
98 2B). Interestingly, *Chromera velia*, a close non-parasitic relative of Apicomplexa whose plastid has
99 retained its photosynthetic capacity [32], has two HCF101 isoforms: one with a predicted transit
100 peptide (potentially addressed to the plastid), and one without (Fig. 1, Fig. S1). A recent study suggests
101 that the plastid-located HCF101 in fact evolved from an ancestral cytosolic HCF101 [23]. This led us to
102 hypothesize that apicomplexan HCF101 would be involved in a cytosolic-related, rather than in a
103 plastid-associated, Fe-S cluster transport function. Additional supporting evidence comes from the
104 characterization of a C-terminal targeting complex recognition (TCR) signal ending with an aromatic
105 residue ([LIM]-[DES]-[WF]) in the clients proteins of the cytosolic Fe-S cluster machinery or their
106 adaptors [33], which can be clearly identified in the apicomplexan HCF101 homologues, as well as in
107 the *C. velia* isoform without transit peptide (Fig. S1).

108 To assess experimentally the localization of TgHCF101, we first tagged an ectopic copy with a C-
109 terminal GFP and observed a cytosolic localization (Fig. S2A), in line with what had been described
110 previously when an additional copy of TgHCF101 bearing a C-terminal Human influenza hemagglutinin
111 (HA) tag was expressed [23]. However, given the potential importance of the C-terminal TCR signal for

112 HCF101 function or localization, we next generated a transgenic cell line in which we modified the 5'
113 region of the *TgHCF101* gene by homologous recombination to replace the endogenous promoter by
114 an inducible-Tet07*SAG4* promoter, and at the same time adding a sequence coding for a N-terminal
115 hemagglutinin (HA) tag (Fig. 1C, D). In this conditional knock-down (cKD) HA-TgHCF101 cell line, the
116 addition of anhydrotetracycline (ATc) can repress transcription of *TgHCF101* through a Tet-Off system
117 [34]. Two independent transgenic clones were obtained and found to behave similarly in the initial
118 phenotypic assays we performed, so only one will be described in details here.

119 Immunoblot analysis showed a N-terminal HA-tagged protein at around 70 kDa (the predicted
120 molecular mass for TgHCF101), and depletion of the protein was efficient upon addition of ATc (Fig.
121 1E). Immunofluorescence assay (IFA) showed a punctate cytosolic signal for TgHCF101, clearly distinct
122 from the apicoplast, and efficiently depleted by the addition of ATc (Fig. 1F). Disruption of the
123 apicoplast-located SUF pathway has a strong impact on the lipoylation of the E2 subunit of the
124 pyruvate dehydrogenase (PDH-E2) by Fe-S-containing lipoate synthase LipA [19,21]. However,
125 depletion of TgHCF101 did not seem to have an impact on the lipoylation profile of PDH-E2 (Fig. S2B).
126 Disruption of the SUF pathway also typically impacts the apicoplast-located isoprenoid synthesis,
127 which involves two Fe-S oxidoreductases (IspG and IspH) and has been shown to have downstream
128 consequences on the glycosylation of proteins involved in parasite motility [21]. We thus assessed the
129 gliding motility of the parasites after TgHCF101 depletion and found that it was only affected after four
130 days of ATc treatment, which might be reflecting long-term impact of TgHCF101 depletion on parasite
131 fitness rather than a direct consequence of apicoplast-related Fe-S cluster synthesis (Fig. S3A, B).

132 Altogether, our results indicate that TgHCF101 is not associated with the apicoplast-located SUF
133 pathway, but localizes to the cytosol instead.

134

135 *TgHCF101 is essential for parasite growth*

136 We next assessed the impact of TgHCF101 depletion on the parasite's lytic cycle: we evaluated the
137 capacity of TgHCF101-depleted tachyzoites (a highly replicative and highly invasive form responsible
138 for the acute form of the disease caused by *T. gondii*) to generate lysis plaques. For this, we infected a
139 monolayer of host cells in absence or continuous presence of ATc for 7 days (Fig. 2A, B). Depletion of
140 TgHCF101 completely prevented plaque formation. While absence of plaques highlights a fitness
141 problem for the parasites, it does not necessarily implies their death: for instance, in response to stress,
142 tachyzoites can convert into a slow-growing and cyst-enclosed persisting stage called bradyzoites
143 (associated with the chronic form of the disease), that can reactivate when they encounter more
144 favourable conditions [35]. We thus performed a similar experiment, in which the ATc was washed out
145 at the end of the 7-day incubation, and then incubated the parasites for an extra 7 days in the absence
146 or presence of ATc before evaluating plaque formation (Fig. 2C). We did not observe any plaques after
147 ATc removal, suggesting that the parasites were not able to recover after 7 days of TgHCF101
148 depletion, likely because they were dead.

149 To assess whether this defect in the lytic cycle is due to a replication problem, cKD HA-TgHCF101
150 parasites were preincubated in ATc for 48 hours and then released mechanically, before infecting new
151 host cells for an additional 24 hours in ATc prior to parasite counting. We noted that incubation with
152 ATc led to an accumulation of vacuoles with fewer parasites (Fig. 2D). To get more precise insights into
153 the impact of TgHCF101 depletion on parasite division, we labelled dividing parasites with inner
154 membrane complex (IMC) protein IMC3 [36] to detect growing daughter cells (Fig. 2E). *T. gondii*
155 tachyzoites develop inside a mother cell by a process called endodyogeny [37] and this division is
156 usually highly synchronous within the same parasitophorous vacuole, yet after two days of ATc

157 treatment vacuoles showed a marked lack of synchronicity for daughter cell budding. Investigation of
158 the consequences of TgHCF101 depletion on developing parasites by electron microscopy highlighted
159 important defects on cytokinesis, although the overall appearance of organelles seemed essentially
160 normal (Fig. 2F). Finally, through propidium iodide labelling and flow cytometer-based analysis of DNA
161 content, we observed that long-term depletion of TgHCF101 led to the emergence of an increasing
162 subpopulation of parasites with sub-1N DNA content, thus smaller than the typical haploid 1N DNA
163 content if the parasites (Fig. 2G), suggesting an impairment in DNA synthesis.

164 Overall, our results indicate that TgHCF101 depletion leads to important and, apparently, irreversible
165 defects in parasite replication and growth.

166

167 *Depletion of TgHCF101 induces stress response mechanisms*

168 Through electron microscopy analysis, we also noticed that the depletion of TgHCF101 induced the
169 appearance of structures resembling lipid droplets (LDs) in several parasites (Fig. 3A). In order to
170 properly quantify this, we used Nile red, a selective fluorescent stain for neutral lipids, and microscopic
171 imaging (Fig. 3B). We noticed a strong increase in both the number and size of LD in cKD HA-TgHCF101
172 parasites incubated for two days with ATc (Fig. 3C, D). To see if this was a common feature induced by
173 abolishing Fe-S synthesis, we quantified LDs in mutants of the mitochondrial (TgISU1) and apicoplast
174 (TgSUFC) pathways [19]. Specific depletion of these proteins did not lead to an increase in LD formation
175 (Fig. S4A, B), indicating it is specific to the depletion of TgHCF101. To assess if the induction of LD
176 formation could play a role in the demise of the parasites, we used T863, a pharmaceutical inhibitor of
177 the acyl coenzyme A:diacylglycerol acyltransferase 1 (DGAT1) enzyme, which is important for storing
178 neutral lipids in cytoplasmic LD [38]. While treatment with T863 efficiently decreased the number of
179 LDs (Fig. S4C, D, E), long term incubation during plaque assays did not allow any recovery in parasite
180 fitness (Fig. S4F). This suggests that LDs are not detrimental to TgHCF101-depleted parasites but
181 instead could be art of an integrated stress response, as they have been shown in other eukaryotes to
182 be upregulated in response to cellular injuries including nutrient-related and oxidative stresses [39].

183 Disrupting proteins involved in Fe-S cluster assembly may have a direct effect on the stability and
184 expression levels of local Fe-S proteins. Thus, to get insights into the effect of TgHCF101 depletion at
185 the molecular level, we performed global label-free quantitative proteomic analyses. Of course, this
186 may also affect downstream cellular pathways or functions, and other pathways may also be
187 upregulated in compensation. cKD HA-TgHCF101 or TATi ΔKu80 parental control parasites were
188 treated for three days with ATc prior to a global proteomic analysis and compared for protein
189 expression. We selected candidates with a $\log_2$(fold change) ≤-0.55 or ≥0.55 (corresponding to a ~1.47-
190 fold change in decreased or increased expression) and a p-value <0.05 (ANOVA, *n*=4 biological
191 replicates) and we completed this dataset by selecting some candidates that were consistently and
192 specifically absent from the mutant cell lines or only expressed in these (Tables S2 and S3). Many
193 higher-expressed proteins were bradyzoite stage-specific and more particularly components of the
194 cyst wall or their cell surface [40,41] (Fig. 4A, B, Table S2). Tachyzoites can convert to the persistent
195 bradyzoite form upon stress, so to check if TgHCF101 depletion was inducing stage conversion we used
196 a lectin from the plant *Dolichos biflorus*, which recognizes the SRS44/CST1 cyst wall glycoprotein in
197 differentiating cysts [42] (Fig. 4C, D). We could see that TgHCF101 depletion induced the appearance
198 of up to 10% of lectin-labelled vacuoles during the first 48 hours of intracellular growth in the presence
199 of ATc. However, when parasites were kept for up to a week in the presence of ATc, the proportion of
200 lectin-positive vacuoles plateaued at 14% and only a very limited number of vacuoles looked like bona

201 fide mature cysts (less than 2% were both lectin-positive and containing more than 2 parasites) (Fig.
202 4E).

203 These data suggest that depletion of TgHCF101 leads to a cellular stress that initiates stage conversion
204 into the bradyzoite stage, but that the differentiation process into mature cysts cannot be completed.

205

206 *Depletion of TgHCF101 affects specifically cytosolic and nuclear Fe-S proteins*

207 The label-free quantitative proteomic analyses also highlighted proteins which were less expressed in
208 absence of TgHCF101. Among them, were a surprisingly large number of rhoptry bulb proteins (Table
209 S3, Fig. S5A). Rhoptries are club-shaped organelles that comprise a narrow tubular neck opening at the
210 anterior pole of the parasite, and a most posterior bulbous part; the proteins secreted from these
211 different sub-compartments are either involved in invasion and parasitophorous vacuole formation,
212 or in the modulation of host cell defenses, respectively [43]. We assessed if there was any major impact
213 of TgHCF101 depletion on rhoptry morphology or function. We performed IFA with anti-armadillo
214 repeats only protein (TgARO), a protein homogenously anchored to the surface of the rhoptry
215 membrane [44], and found no particular defect in rhoptry morphology or positioning (Fig. S5B).
216 Quantification of intracellular evacuoles (rhoptry-secreted vesicular clusters) did not indicate any
217 particular problem in the secretory capacity of the organelles upon TgHCF101 (Fig. S5C). Finally, we
218 assessed by immunoblot the expression profile of one of the potentially less-expressed rhoptry bulb
219 protein but found only a slight alteration in the expression profile (a modest increase in the non-
220 mature from of the protein), but not in the overall amount of protein (Fig. S5D). We conclude that
221 although TgHCF101 depletion may lead to a secondary impact on rhoptry content, it does not
222 massively impact organelle morphology or secretory function.

223 Given the potential implication of TgHCF101 in the biogenesis of Fe-S proteins, we also specifically
224 searched for putative Fe-S proteins in the less expressed proteins highlighted by the label-free
225 quantitative proteomic analysis. We have previously estimated the Fe-S proteome using a
226 computational predicting metal-binding sites in protein sequences [45], which, coupled with the data
227 from global mapping of *T. gondii* proteins subcellular location by HyperLOPIT spatial proteomics [46],
228 allows predicting client proteins present in the mitochondrion, apicoplast or cytosolic [19]. We found
229 three Fe-S proteins that were less expressed upon TgHCF101 depletion (Fig. 5A). Interestingly, they
230 were all connected to the CIA pathway as they were NAR1, a Fe-S carrier to the CIA core machinery
231 [15], and two Fe-S proteins depending on the CIA machinery [47]: ABCE1 (Rli1 in yeast) a cytosolic
232 ribosomal recycling factor and NTHL1, a nuclear DNA base-excision repair enzyme. In order to verify
233 the proteomics data, we tagged TgABCE1 with a myc epitope in the context of the cKD HA-TgHCF101
234 mutant (Fig. S6A, B). IFA showed a decrease in the cytosolic TgABCE1 signal (Fig. 5B), which was
235 supported by quantitative immunoblot analysis indicating a significant decrease in TgABCE1 upon
236 treatment of cKD HA-TgHCF101 mutant with ATc (Fig. 5C, D).

237 These results indicate that perturbing TgHCF101 expression has consequences on proteins of the CIA
238 machinery or depending on this machinery for the assembly of their Fe-S cluster.

239

240 *TgHCF101 is likely a Fe-S transfer protein of the CIA complex.*

241 To get further insights on the role played by TgHCF101 in the CIA machinery, we next performed co-
242 immunoprecipitations (co-IPs) and mass spectrometry identification of associated proteins, comparing
243 lysates of cKD HA-TgHCF101 parasites grown in the presence of ATc or not (Table S4). Strikingly, we

244 pulled-down all three *T. gondii* homologues of the core components of the CTC: MET18, CIA1 and AE7
245 (a MIP18 family protein) (Fig. 6A). We managed to tag the TgCIA1 protein with a myc epitope tag in
246 the context of the HA-tagged TgHCF101 cell line (Fig. S6C, D) and performed a reverse IP by which we
247 managed to specifically pull-down TgHCF101, confirming their interaction (Fig. 6B). It should be noted
248 that this result was only obtained when this experiment was performed after chemical crosslinking,
249 suggesting a possibly indirect or transient interaction between the proteins.

250 Another interesting candidate that was found co-immunoprecipitated with TgHCF101 was TgABCE1,
251 strengthening the possibility of an important relationship between the two proteins. We next
252 performed a reverse IP and could recover small amounts of TgHCF101 co-eluting specifically with
253 TgABCE1 (Fig. 6C). To further investigate this potential interaction, we performed yeast two-hybrid
254 assay, based on interaction-dependent transactivation of the HIS3 reporter gene (Fig. 6D). This
255 experiment confirmed that there is a direct interaction between TgHCF101 and TgABCE1, and
256 highlighted a particularly strong interaction, as it was retained when using 3-aminotriazole, a
257 competitive inhibitor of the HIS3 gene product (Fig. 6D). This confirms that TgABCE1 is likely a client
258 protein of TgHCF101. Given the known implication of ABCE1 in translation, we next evaluated the
259 impact of TgHCF101 depletion on translation by using a puromycin-based assay (Fig. 6E). Puromycin
260 can mimic aminoacyl-tRNA and becomes covalently attached to nascent peptides, thereby allowing
261 the evaluation of protein elongation rates with an anti-puromycin antibody [48]. Using this method,
262 we could show that TgHCF101 depletion leads to a modest but a significant decrease in the overall
263 translation rate (Fig. 6E, F).

264 Together, these results suggest that TgHCF101 acts as a Fe-S transfer protein to the translation
265 regulator TgABCE1.

266

267 **Discussion**

268 Fe-S clusters are universal among living organisms, where they play key roles in many important
269 biological processes as cofactors of proteins involved for instance in housekeeping functions like
270 respiration, photosynthesis, as well as genome expression or maintenance [6]. These cofactors were
271 acquired early during evolution, and thus they played a fundamental role in the evolution of the
272 eukaryotic cells as they were inherited through endosymbiosis to organelles such as the mitochondrion
273 or plastids [5]. Different Fe-S cluster synthesis pathways show globally-conserved mechanistic and
274 biochemical features to assemble and transfer the clusters prior to transferring them to client proteins
275 [7]. However, beyond a core Fe-S synthesizing machinery, given the large diversity of eukaryotic
276 lineages, it is likely that some have evolved some specific features.

277 For instance proteins of the MRP/NBP35 family (NBP35, Cfd1, Ind1 and HCF101), have in common a
278 central P-loop NTPase domain [26], but are either involved in scaffolding or transfer of Fe-S clusters at
279 specific sub-cellular locations like the mitochondrion, plastid, or in the cytosol [12,24,25,49]. Presence
280 of MRP family members in bacteria that are able to bind Fe-S clusters point to ancient and conserved
281 function linked to Fe-S biogenesis for these proteins [50]. Another feature shared by members of this
282 family is their ability to form homo- or hetero-dimers bridging one Fe-S cluster at their interface
283 through two conserved and functionally essential Cys residues [51]. Interestingly, HCF101 also presents
284 at its N-terminal a MIP18-like domain that constitutes most of a bacterial protein called SufT that is
285 involved in Fe-S maturation [28,50,52], as well as a C-terminal domain whose function is not yet
286 defined (DUF971). The presence of additional domain besides the conserved NTPase core domain in
287 members of the MRP family like HCF101 suggests a potential complexification linked to more
288 specialized functions. Another clue of evolutionary specialization comes from the different localization

289 of protein isoforms in different species, hinting for a possible association to different Fe-S cluster
290 biogenesis machineries. While HCF101 was initially characterized as a chloroplast-associated protein
291 with a specialized function in maintaining PSI homeostasis, a recent study suggested a wider diversity
292 in localization for HCF101 paralogs across eukaryotes, especially in alveolates, with isoforms
293 potentially localizing to the mitochondrion in *Tetrahymena* or in the cytosol in *T. gondii* [23]. Our study
294 confirms that although *T. gondii* harbors a plastid, TgHCF101 is expressed in the cytosol (Fig. 1F, Fig.
295 S2B), which is consistent with the absence of photosynthesis-related pathways in *T. gondii*. Our study
296 establishes for the first time that the cytosolic expression of TgHCF101 is functionally related to the
297 CIA pathway (Fig. 7).

298 Previous functional investigations of the CIA pathway in *T. gondii* focused on TgABCB7, a mitochondrial
299 transporter presumably involved in providing a sulfur-containing precursor for further processing by
300 the cytosolic Fe-S assembly machinery [53] and on TgNBP35, a Fe-S scaffolding protein of the CIA that
301 displays an unusual association with the outer mitochondrial membrane in the parasites [20]. These
302 two proteins are quite upstream in the CIA machinery, and imply that the assembly of cytosolic Fe-S
303 clusters likely happens at the cytosolic face of the mitochondrion in *T. gondii*, and then probably shuttle
304 through the *T. gondii* NAR1 homologue to the CTC for subsequent transfer to client proteins (Fig. 7).
305 CTC proteins have so far not been functionally investigated in the parasite, but both TgABCB7 and
306 TgNBP35 are essential for parasite growth and were both shown to be important for TgABCE1 stability
307 [20,53]. Combining genome-wide data for potential essentiality and localization [46,54] to metal-
308 binding site prediction algorithms [45], our previous assessment of the putative *T. gondii* cytosolic and
309 nuclear Fe-S proteome highlighted proteins involved in key functions like genome reparation and
310 maintenance, mRNA synthesis and protein expression [19]. It is thus unsurprising to see that *T. gondii*
311 mutants of the CIA pathway are severely impaired in growth. Our quantitative proteomics analysis of
312 the TgHCF101 mutant did not reveal an impact on many nuclear or cytosolic Fe-S proteins, which may
313 indicate that this protein could be involved in cluster transfer to a reduced subset of Fe-S proteins.
314 Besides the decrease in abundance of TgNAR1, strengthening the evidence of TgHCF101 involvement
315 in the CIA pathway, quantitative proteomics data revealed a decrease in two potential client Fe-S
316 proteins: TgABCE1 and TgNTHL1. While we could establish a direct association of TgHCF101 with
317 TgABCE1 by co-immunoprecipitations and yeast two hybrid (Fig. 6A, C, D), we did not manage to tag
318 TgNTHL1 to perform co-immunoprecipitations and did not obtain proof of a direct TgHCF101/TgNTHL1
319 interaction by yeast two hybrid.

320 Although it is not firmly established that TgNTHL1 is a client protein of TgHCF101, our phenotypic
321 analysis of TgHCF101-depleted parasites revealed cell division and DNA replication problems (Fig. 2D,
322 G) that might result from an impact on Fe-S protein-mediated DNA maintenance. In addition, through
323 perturbation of TgABCE1 function, we measured a decrease in the overall translation rate in the
324 parasites (Fig. 6E, F), that could contribute to their decreased fitness and growth problems. Upon two
325 days of TgHCF101 depletion, parasites also started to display an accumulation of LDs (Fig. 3). LDs are
326 known to be induced as part of an integrated stress response to cellular injuries and may be induced
327 in conditions such as oxidative stress [39]. For instance, during the particular Fe-induced cell death
328 called ferroptosis iron excess, combined to oxygen, leads to the accumulation of reactive oxygen
329 species (ROS), leading to subsequent peroxidation of lipids, which in turn induces the accumulation of
330 lipid droplets that act as antioxidant organelles to control polyunsaturated fatty acid storage in
331 triglycerides in order to reduce membrane lipid peroxidation [55]. Although it is possible that
332 perturbation of the CIA pathway created local imbalance in cytosolic Fe concentration and ROS-
333 dependent stress that contributed to the demise of the parasites, it is to note that our previous work
334 has shown that general Fe deprivation has a similar LD-inducing effect on the parasites [56]. So,
335 altogether this may rather suggest that specific CIA-dependent Fe-S protein(s) that remain to be

336 determined could be involved in regulating LDs. Even more so than the induction of LDs, initiation of
337 stage conversion to the bradyzoite persistence form is a hallmark of the stress response in *T. gondii*
338 [35]. Upon depletion of TgHCF101 we could detect early signs of differentiation (Fig. 4), but the
339 parasites were largely unable to progress to full stage conversion and died instead (Fig. 2C, Fig. 4E).
340 Importantly, overall our data show that TgHCF101 is essential for parasite viability, and although our
341 findings point towards an involvement of this protein in the eukaryote-conserved CIA pathway, its
342 specific absence from the mammalian hosts of the parasite makes it a good potential drug target. This
343 calls for further structure/function studies of TgHCF101 in order to potentially design specific
344 inhibitors.

345 There is a vast repertoire of Fe-S client proteins with a diverse range of structures and roles, and one
346 important conundrum remaining in the Fe-S research field is resolving functional specificity of the
347 transfer proteins during the addition of Fe-S to apoproteins. Key investigations in budding yeast
348 allowed the identification of mutually exclusive sub-complexes of the CTC that can transfer Fe-S
349 clusters to different proteins [47,57]. In particular, it was shown that a complex of two small proteins,
350 Yae1 and Lto1, functions as a target-specific adaptor to recruit the yeast homologue of ABCE1 (called
351 Rli1) to the generic CIA machinery [57]. These adaptor proteins are well-conserved in phylogenetically-
352 close opisthokonts like humans, in which they have also been shown to be important for ABCE1
353 maturation [58,59]. However, Yae1 and Lto1 are clearly not conserved across all eukaryotes but found
354 essentially in fungi, metazoan and plants (Fig. S7), and thus noticeably they do not seem to have
355 homologues in the Alveolata superphylum that includes apicomplexan parasites. So, while ABCE1 is
356 arguably one of the most conserved proteins in evolution and is universally present in all eukaryotes
357 [60], the factors driving its CIA-dependent maturation seem phylogenetically divergent. We have now
358 established that in *T. gondii*, HCF101 is associated to the CTC and likely plays that role in this organism.
359 Given sequence conservation of HCF101 homologs, it is also likely to be the case in other apicomplexan
360 parasites and even possibly in one isoform present in the photosynthetic relative *C. velia* (Fig. 1A, B,
361 Fig. S1). Our results highlight the complex evolutionary adaptation that accompanied the maturation
362 of highly complex eukaryotic Fe-S protein and calls for in-depth structural analysis of this interaction.
363 Not only this would provide invaluable evolutionary insights into the molecular machinery supporting
364 Fe-S cluster transfer, but also may provide new prospects for interfering specifically with an essential
365 function, as a new strategy against apicomplexan-caused diseases.

366

367

368

369

370

371 **Methods**

372 *Cell culture*
373 *Toxoplasma gondii* RH tachyzoites and derived transgenic cell lines generated in this study were
374 routinely maintained through passages in human foreskin fibroblasts (HFFs) monolayer (ATCC CRL-
375 1634). HFFs and parasites were cultured in standard Dulbecco's Modified Eagle's Medium (DMEM,
376 supplemented with 5% decomplemented fetal bovine serum (FBS), 2 mM L-glutamine, 100 U/mL
377 penicillin and 100 µg/mL streptomycin (Gibco) in a controlled atmosphere at 37°C and with 5% CO_2.
378 For immunoprecipitation assays, parasites were grown in Vero cells (ATCC, CCL-81) in the same
379 conditions as for the HFFs.

380 Transgenic cell lines were generated in the TATi ΔKu80 genetic background line lacking the *Ku80* gene
381 and expressing the TATi transactivator required for the TetOff system [61]. For positive selection of
382 transgenic parasites bearing resistance cassettes for expressing dihydrofolate reductase thymidylate
383 synthase (DHFR-TS) or chloramphenicol acetyltransferase (CAT) were grown with 1 µM pyrimethamine
384 or 20 µM chloramphenicol (Sigma-Aldrich, SML3579, C0378), respectively. Conditional depletion in the
385 TetOff conditional knockdown lines was achieved by incubation with 0,5 µg/mL anhydrotetracycline
386 (ATc, Fluka 37919) for the indicated duration of the assay.
387
388 *Bioinformatic analyses*
389 Genomic and protein sequences were retrieved from http://www.toxodb.org or
390 https://www.ncbi.nlm.nih.gov/protein/. Protein alignments were performed from eukaryotic MRP
391 family proteins (Table S1), whose sequences were obtained from Grosche et al. [62], and updated by
392 manual curation using the MUltiple Sequence Comparison by Log-Expectation (MUSCLE) algorithm of
393 the Geneious software suite v 6.1.8 (http://www.geneious.com). Phylogenetic trees were constructed
394 using the MEGA software v11.0.13 (https://www.megasoftware.net/), using the unweighted paired
395 group mean arithmetic (UPGMA) method, with Poisson model for amino acid substitution.
396 Transit peptide and sub-cellular localization predictions were performed using the ChloroP 1.1
397 (https://services.healthtech.dtu.dk/services/ChloroP-1.1/), IPSORT (http://ipsort.hgc.jp/), and
398 Localizer 1.0.4 (http://localizer.csiro.au/) algorithms. Domain searches were performed using the
399 Interpro database (https://www.ebi.ac.uk/interpro/).
400
401
402 *Generating a GFP-tagged TgHCF101 cell line*
403 cDNA corresponding to the *TgHCF101* gene (TGGT1_318590) was amplified by PCR with primers
404 ML4715 and ML4716 (all primers used in the present study are listed in Table S5) and sub-cloned using
405 XhoI and KpnI into the pEZS-NL vector (D. Ehrhardt,
406 https://deepgreen.dpb.carnegiescience.edu/cell%20imaging%20site%20/html/vectors.html) for a C-
407 terminal GFP fusion. The TgHCF101-GFP cassette was them amplified by PCR using the ML4817 and
408 ML4818 primers and cloned using BclI and EcoRV in a BlgII/EcorV-digested pTUB-IMC1-TdT vector [63]
409 to drive the expression from a tubulin promoter. Tachyzoites were transfected with 100 µg of plasmid
410 and observed by fluorescence microsocopy.
411
412 *Generating a conditional TgHCF101 knock-down cell line*
413 To generate the construct for the tetracyclin-regulated conditional depletion of TgHCF101 and add a
414 N-terminal HA tag, we digested the DHFR-TetO7Sag4 plasmid [63] by BglII and inserted a fragment
415 coding for a single HA tag generated through hybridization of the ML4924 and ML4925
416 oligonucleotides. Then, a fragment corresponding to the 5' coding part of TgHCF101 was amplified by
417 PCR with primers ML4926 and ML4927 and inserted after digesting with BglIU and NotI to yield the
418 DHFR-TetO7Sag4-TgHCF101 plasmid. The TATi ΔKu80 cell line was transfected with 80 µg of the BsiWI-
419 linearized DHFR-TetO7Sag4-TgHCF101 plasmid. Transgenic parasites, named cKD HA-TgHCF101, were
420 selected with pyrimethamine and cloned by limiting dilution. Positive clones were verified by PCR with
421 primers ML1771 and ML6043.
422
423 *Tagging of ABCE1 and CIA1 in the TgHCF101 knock-down background*
424 A CRISPR-based strategy was used to C-terminally tag proteins of interest in the cKD HA-TgHCF101
425 background. Guide RNAs (gRNAs) targeting the C-terminal end of the gene of interest were selected
426 using CHOP-CHOP tool (https://chopchop.cbu.uib.no/). gRNAs were cloned into the pU6-Cas9
427 Universal Plasmid (Addgene, 52694) using BsaI. Donor DNA was amplified by PCR using the high fidelity
428 KOD DNA polymerase (Novagen) to amplify a fragment containing the tag and the resistance cassette,
429 using the pLIC-myc-CAT plasmid as a template, adding at both ends 30-nucleotide overhangs
430 homologous to the C-terminal region of the gene of interest for homologous recombination. *TgABCE1*
431 (TGGT1_216790) tagging was performed by using primers ML5126 and ML5127 for the gRNA and

432 ML5128 and ML5129 to amplify donor DNA, yielding the cKD HA-TgHCF101 TgABCE1-myc cell line.
433 Integration of the construct was controlled by PCR using GoTaq DNA polymerase (Promega) with
434 primers ML6115 and ML4310. *TgCIA1* (TGGT1_313280) tagging was performed by using primers
435 ML5932 and ML5933 for the gRNA and ML5934 and ML5935 to amplify donor DNA, yielding the cKD
436 HA-TgHCF101 TgCIA1-myc cell line. Integration of the construct was controlled by PCR using GoTaq
437 DNA polymerase (Promega) with primers ML5936 and ML4310.
438
439 *Immunofluorescence assays*
440 For immunofluorescence assays (IFA), coverslips seeded with HFFs were infected by *T. gondii*
441 tachyzoites. Intracellular parasites and host cell monolayer were then fixed with 4% (w/v)
442 paraformaldehyde (PFA, diluted in phosphate-buffered saline -PBS-) for 20 minutes. After fixation, cells
443 were permeabilized with 0.3% (v/v) Triton X-100 (diluted in PBS) for 10 minutes. Coverslips were
444 blocked with 2% (w/v) bovine serum albumin (BSA) for 1h prior to immunolabelling with primary
445 antibody for 1 hour. After 3 washes in PBS, corresponding secondary antibody was incubated for 1
446 hour. Coverslips were finally incubated with 1 µg/mL 4,6-diamidino-2-phenylindole (DAPI) for 5
447 minutes before 3 washes in PBS and, lastly, mounted using Immu-Mount (ThermoFisher) onto
448 microscope slides. Primary antibodies used were prepared in 2% BSA (diluted in PBS) and used at the
449 following concentrations: rat monoclonal anti-HA (1:1000, 3F10 Roche), mouse monoclonal anti-myc
450 (1:100, 9E10 Sigma), rabbit anti-IMC3 (1:1000) [64], mouse anti-SAG1 (T41E5, 1:1000) [65], rabbit anti-
451 armadillo repeats only (ARO, 1:1000) [44]. Cysts were stained with biotin labelled *Dolichos Biflorus*
452 lectin (1:300, Sigma L-6533) and detected with FITC-conjugated streptavidin (1:300, Invitrogen,
453 SNN1008). Lipid droplets were detected with Nile Red (1 µg/mL, Sigma 72485).
454 All images were acquired at the Montpellier Ressources Imagerie (MRI) facility. Observations were
455 performed with a Zeiss AxioImager Z1 epifluorescence microscope equipped with a Zeiss Axiocam
456 MRm CCD camera and 63X/1.4 or 100X/1.4 Oil Plan Achromat objective. Images were processed on
457 Zen Blue v3.6 (Blue edition) software (Zeiss). Z-stack acquisitions were processed by maximum
458 intensity orthogonal projection when assessing lipid droplets number and area. Adjustments of
459 brightness and contrast were applied uniformly and paired images were acquired with the same
460 exposure time.
461
462 *Plaque and replication assays*
463 The lytic cycle of tachyzoites was assessed by plaque assay as described previously [56]. Briefly,
464 tachyzoites from the cKD HA-TgHCF101 transgenic cell line or parental strain (TATi ΔKu80) were
465 allowed to invade monolayers of HFFs in the presence or absence of ATc. Parasites were cultivated for
466 7 days at 37°C and 5% CO_2 and fixed with 4% (w/v) PFA (diluted in PBS) for 20 minutes. Cells were
467 stained with 0.1% crystal violet solution (V5265, Sigma-Aldrich), washed and air-dried before imaging
468 on an Olympus MVX10 microscope. For the reversibility assay, drug washout was carefully performed
469 after 7 days of ATc pre-treatment and cultures were kept for another 7 days of growth, non-treated
470 control conditions were also infected at this timepoint.
471 For replication assay, parasites were pre-treated in flasks for 48 hours with ATc and extracellular
472 parasites were allowed to invade HFF monolayer on coverslips for another 24 hours before being fixed
473 and performing parasites immunodetection by IFA with mouse anti-SAG1 antibody as described
474 before. The number of parasites per vacuole was scored. Independent experiments were conducted
475 three times, and 200 vacuoles were counted for each condition.
476
477 *Immunoblotting and antibodies*
478 Protein extracts were prepared from 10^7 extracellular parasites resuspended in Laemmli buffer at a
479 final concentration of 10^6 parasites/µL. Extracts were treated with benzonase to remove DNA from
480 samples and resolved by SDS-PAGE before being transferred on nitrocellulose membrane for
481 subsequent protein detection. Primary antibodies used for immunodetection were resuspended at
482 their respective working concentration in 5% (w/v) milk in TNT buffer (0.1 M Tris-HCl, pH 7.6, 0.15 M
483 NaCl, 0.05%, Tween 20). Antibodies used in this study for immunoblot detection were rat anti-HA

484 (1:1000, Roche), mouse anti-myc (1:100, Sigma), mouse anti-SAG1 (1:50, hybridoma), mouse anti-actin
485 (1:25, hybridoma) [66], mouse anti-ROP7 (1:1000, T43H1) [67], mouse anti-puromycin (1:1000,12D10,
486 MABE943 Sigma) and rabbit anti-lipoic acid (1:500, ab58724 Abcam).
487
488 *Puromycin labelling*
489 Strains of interest were grown for 3 days in the presence or absence of ATc. Freshly egressed parasites
490 were filtered on 40µm Cell Strainer (VWR, 723-2757). After filtration and counting, parasites were
491 treated with puromycin (100 µg/mL, puromycin dihydrochloride, Sigma) for 15 minutes at 37°C and
492 5% CO_2. For translation inhibition control, parasites were treated with cycloheximide (100 µg/mL,
493 Sigma) for 10 minutes prior to puromycin incubation. After treatment, parasites were washed in DPBS
494 (Dulbecco's phosphate-buffered saline, Gibco) and collected by centrifugation. Pellet was resuspended
495 in Laemmli buffer and separated on Mini-Protean TGX Stain-free gels 12% (BioRad) activated by a UV-
496 induced 1-minute reaction to produce tryptophan residue fluorescence in order to allow for global
497 protein quantification, following manufacturer instructions. Proteins were then transferred to
498 nitrocellulose membrane for immunodetection using mouse anti-puromycin (1:1000,12D10, MABE943
499 Sigma) and mouse anti-actin (1:25, hybridoma). Total protein content is assessed by Stain-free
500 detection and puromycin signal is detected with secondary antibody mouse coupled with alkaline
501 phosphatase. Both signals were quantified by densitometry using the ImageJ software.
502
503 *Electron microscopy*
504 Parasites were pretreated with ATc for 48h and allowed to reinvade for 24h in the presence of ATc.
505 Untreated parasites were used as a control for normal morphology. Cells were then fixed with 2.5%
506 glutaraldehyde in cacodylate buffer 0.1 M pH7.4. Coverslips were subsequently processed using a
507 Pelco Biowave pro+ (Ted Pella). Samples were postfixed in 1% OsO4 and 2% uranyl acetate, dehydrated
508 in acetonitrile series and embedded in Epon 118 using the following parameters: Glutaraldehyde (150
509 W ON/OFF/ON 1-min cycles); two buffer washes (40 s 150 W); OsO4 (150 W ON/OFF/ON/OFF/ON 1-
510 min cycles); two water washes (40 s 150 W); uranyl acetate (100 W ON/OFF/ON 1-min cycles);
511 dehydration (40 s 150 W); resin infiltration (350 W 3-min cycles). Fixation and infiltration steps were
512 performed under vacuum. Polymerization was performed at 60°C for 48 hr. Ultrathin sections at 70
513 nM were cut with a Leica UC7 ultramicrotome, counterstained with uranyl acetate and lead citrate and
514 observed in a Jeol 1400+ transmission electron microscope from the MEA Montpellier Electron
515 Microscopy Platform. All chemicals were from Electron Microscopy Sciences, and solvents were from
516 Sigma.
517
518 *Label-free quantitative proteomics*
519 Parasites from the TATi ΔKu80 and cKD HA-TgHCF101 cell lines were treated for 72 hours in HFF seeded
520 in T75 cm^2 flasks. After suitable incubation, parasites were released from host cells with a cell scrapper
521 and passed through a 25G needle before filtration on a fiber glass wool column. Parasites were pelleted
522 and washed in Hank's Balanced Salt Solution (HBSS, Gibco). Parasites were resuspended in lysis buffer
523 (1% SDS, 50mM Tris HCL pH 8, 10mM EDTA pH 8) and protein quantification was determined with the
524 bicinchoninic acid kit (Abcam). For each condition, 20 µg of protein resuspended in Laemmli buffer
525 were resolved on a 10% SDS-PAGE for 35 minutes at 100V. Proteins were fixed with a combination of
526 acetic acid and ethanol and stained in PageBlue Protein Staining Solution (ThermoScientific). Each lane
527 was cut in three identical pieces which were digested with trypsin and peptide extraction was done as
528 previously described [68].
529 LC-MS/MS experiments were performed using an Ultimate 3000 RSLC nano system (ThermoFischer)
530 interfaced online with a nano easy ion source and an Exploris 240 Plus Orbitrap mass spectrometer
531 (ThermoFischer). The .raw files were analyzed with MaxQuant version 2.0.3.0 using default settings
532 (PMID: 19029910). The minimal peptide length was set to 6. The files were searched against the *T.*
533 *gondii* proteome (March 2020, https://www.uniprot.org/proteomes/UP000005641-8450). Identified
534 proteins were filtered according to the following criteria: at least two different trypsin peptides with
535 at least one unique peptide, an E value below 0.01 and a protein E value smaller than 0.01 were

536 required. Using the above criteria, the rate of false peptide sequence assignment and false protein
537 identification were lower than 1%. Proteins were quantified by label-free method with MaxQuant
538 software using unique and razor peptides intensities [69]. Statistical analyses were carried out using
539 RStudio package software. The protein intensity ratio (protein intensity in mutant/protein intensity in
540 parent) and statistical tests were applied to identify the significant differences in the protein
541 abundance. Hits were retained if they were quantified in at least three of the four replicates in at least
542 one experiment. Proteins with a significant ($p < 0.05$ or 0.01 with or without Benjamini correction)
543 quantitative ratio were considered as significantly up-regulated and down-regulated respectively.
544 Volcano plots were generated with the Perseus software v2.0.7.0 (https://maxquant.net/perseus/).
545 Perseus was also used for hierarchical clustering of bradyzoite- and tachyzoite-specific surface antigens
546 of the SRS family using RNAseq data of Hehl et al. [70], available on www.Toxodb.org.
547
548 *Co-immunoprecipitation and mass spectrometry identification*
549 Parasites of the cKD HA-TgHCF101 transgenic cell line were treated for 3 days in the presence or
550 absence of ATc in T175 cm^2 seeded with Vero cells. After treatment, intracellular parasites were
551 released by scraping of the host cells and three passages through a 26G needle. To eliminate cell host
552 debris, parasites were filtered through fiber glass wool and harvested by centrifugation at 650g for 5
553 min and washed three times in DPBS (Gibco). Parasites were resuspended in lysis buffer (1%NP40, 50
554 mM Tris-HCl pH8, 150 mM NaCl, 4 mM EDTA, supplemented with cOmplete Mini protease inhibitors
555 mix (Roche)) and incubated overnight at 4°C on a rotating wheel. Centrifugation of insoluble material
556 was performed at 13500g for 30 min at 4°C. The supernatant was transferred to a tube containing 50µL
557 of anti-HA magnetic beads (ThermoFischer, 88836) for 4h at 4°C on a rotating wheel. The depleted
558 fraction was then removed and beads were washed 5 times with lysis buffer. For the elution of
559 immunoprecipitated proteins, beads were incubated in 50 µL of HA peptide solution at 2 mg/mL
560 (ThermoFischer, 26184) for 1h at 37°C on a rotating wheel. The eluted proteins were mixed with
561 Laemmli buffer and resolved on a 10% SDS-Page for 35 minutes at 100V. In-gel proteins were fixed
562 with a combination of acetic acid and ethanol and stained with PageBlue Protein Staining Solution
563 (ThermoScientific). Each lane was cut in three identical pieces which were digested with trypsin,
564 peptide extraction was done as previously described [68] and mass spectrometry identification was
565 performed as described for label-free quantitative proteomic.
566 Proteomic data were analyzed on R following the publicly available script of DEP analysis package
567 (https://github.com/arnesmits/DEP, v.1.7.1). The following parameters were used for differential
568 expression analysis: dataset was normalized by variance-stabilizing transformation and missing values
569 were imputed via MNAR (missing not at random) method, the fold change cutoff was set at 1.5 and p-
570 value at 0.05. Statistical analyses were performed by a differential enrichment test based on protein-
571 wise linear models and empirical Bayes statistics [71] and p-values were adjusted by the Benjamini-
572 Hochberg correction.
573 Validation of co-immunoprecipitation mass spectrometry results was performed by immunoblotting.
574 C-terminally c-myc tagged candidates in the cKD HA-TgHC101 background were grown in the presence
575 or absence of ATc for 48h. Parasites were harvested and subjected to co-immunoprecipitation using
576 myc-Trap agarose beads (Chromotek, yta-20) following manufacturer's instructions. Cross-linking of
577 proteins was performed prior to co-immunoprecipitation for the cKD HA-TgHCF101 CIA1-myc cell line
578 using 1% (w/v) PFA (diluted in PBS) for 5 minutes at room temperature and quenched with 125 mM
579 ice-cold glycine. Immunoprecipitated proteins were then resolved on 10% SDS-Page prior to
580 immunoblot analysis.
581
582 *Yeast two-hybrid*
583 RNA was extracted from parasites using NuceloSpin RNA kit (Macherey-Nagel). cDNA was obtained
584 using SuperScript III First Strand Synthesis SuperMix for RT-qPCR (Invitrogen) using oligodT and
585 following the manufacturer's instructions. Specific cDNAs were subsequently amplified using KOD DNA
586 polymerase (Novagen). Cloning was performed with In-Fusion HD cloning kit (Takara) for each
587 candidate into pGADT7 and pGBKT7 vectors (Clontech, Takara Bio) to allow expression of AD-(Gal4

588 activation domain) and BD-(Gal4 DNA binding domain) fusion proteins, respectively. Primers were
589 designed using the InFusion Cloning Primer Design Tool (https://takarabio.com/) and are listed in Table
590 S5.
591 All experiments were performed in the Gal4-based yeast two-hybrid (Y2H) reporter strain YRG2
592 (MATα, *ura3-52*, *his3-200*, *ade2-101*, *lys2-801*, *leu2-3*, *112*, *trp1-901*, *gal4-542*, *gal80-538*,
593 *lys2*::UAS_{GAL1}-$TATA_{GAL1}$-HIS3, URA3::$UAS_{GAL4,17MERS(x3)}$-$TATA_{CYC1}$-LacZ) (Stratagene, Agilent). Yeast cells
594 were co-transformed by pGAD/pGBK construct pairs and selected on plates containing the minimal
595 YNB medium (0.7% Yeast Nitrogen Base medium without amino acids, 2% glucose, 2% Difco agar)
596 supplemented with histidine (H), adenine (A), Lysine (K), and uracil (U) according to Gietz and Woods
597 [72]. For all Y2H interaction assays, individual co-transformed colonies were cultured on liquid
598 YNB+HUKA, adjusted to an OD_{600} of 0.05 and dotted on YNB+UKA plates containing (+His plates) or
599 missing (-His plates) histidine (7 µL per dot). Plates were incubated at 30°C, and cell growth was
600 recorded after 5 days. Constructs pairs including empty vectors (AD-fusion + empty BD, or empty AD +
601 BD-fusion) were tested first to evaluate the capacity of each protein of interest to transactivate the
602 *HIS3* reporter gene in the absence of interactor, and to determine the appropriate 3-aminotriazole
603 (3AT) concentration required to abolish false interactions. True positive interactions were visualized
604 as cells growing on YNB+UKA in the absence of histidine (-his plates) and eventually in the presence of
605 3AT if required. Increasing 3AT concentrations were also used to challenge the strength of positive
606 interactions. For all assays, at least three independent transformations per construct pairs were
607 performed.
608
609 *DNA content analysis*
610 DNA content analysis by flow cytometry was performed as described previously [73]. Parasites from
611 the cKD HA-TgHCF101 strain and from the background line TATi ΔKu80 were treated for up to four days
612 in the presence or absence of ATc. Extracellular parasites were removed by washing with HBSS and
613 intracellular parasites were released from host cell by scraping with a cell scraper (VWR, 734-2602),
614 passages through 26G needles and finally filtered on a fiber glass wool column. Parasites were then
615 fixed overnight in a solution of 70% ethanol and 30% PBS at 4°C. After fixation, parasites were washed
616 in PBS and stained with a 30 µM propidium iodide solution for 30 min. Parasites DNA content was then
617 analyzed by flow cytometry with an Aurora cytometer (Cytek) from the MRI facility.
618
619 *Gliding motility assay*
620 Parasites from the parental TATi ΔKu80 and the cKD HA-TgHCF101 transgenic cell lines were grown in
621 the presence or absence of ATc for up to 4 days. 1.10^6 freshly egressed parasites were harvested and
622 resuspended in 400µL motility buffer (155 mM NaCl, 3 mM KCl, 2 mM $CaCl_2$, 1 mM $MgCl_2$, 3 mM
623 NaH_2PO_4, 10 mM HEPES, 10 mM glucose) and 100 µL of the suspension was immediately placed on
624 poly-L-lysine coated slides and incubated at 37°C for 15 min. Unattached parasites were removed by
625 performing three washes with PBS. Finally, attached parasites were fixed with 4% (w/v) PFA and
626 stained with anti-SAG1 antibody. Trails length were captured with a 63x objective on a Zeiss AXIO
627 Imager Z2 epifluorescence microscope and were quantified using the NeuronJ plug-in on the ImageJ
628 software as described previously [74].
629
630 *Rhoptry secretion assay*
631 Rhoptry secretion was quantified by performing an evacuole assay [75]. Parasites from the cKD HA-
632 TgHCF101 strain and cKD TgARO strain were grown in the presence or absence of tetracycline for up
633 to 72 hours. Freshly egressed parasites were then pre-treated for 10 min in DMEM supplemented with
634 1 µM cytochalasin D (cytD), an inhibitor of actin polymerization. Parasites were allowed to secrete
635 their rhoptry content as they were put in contact with HFF cells for 15 min in the presence of cytD at
636 37°C. Parasites and HFF cells were then immediately fixed with 8% (w/v, in PBS) PFA, permeabilized
637 with 0.1% Triton X-100 and stained with anti-ROP1 and anti-SAG1 to detect secreted rhoptry material
638 and parasites, respectively. For each technical replicate, 20 fields were quantified and three technical
639 replicates were performed for each of the three biological replicates.

640
641 *Statistical analyses*
642 Statistical analyses were generally performed with the Prism 8.3 software (Graphpad). For proteomics
643 experiments, statistics were performed with version 4.2.1 of the R package (2022-06-23,
644 https://www.R-project.org/) using the Differential Enrichment analysis of Proteomics Data (DEP,
645 v.1.23.0) package. Unless specified, values are expressed as means ± standard deviation (SD).
646

647 **Data availability**

648 All raw MS data and MaxQuant files generated have been deposited to the ProteomeXchange
649 Consortium via the PRIDE partner repository (https://www.ebi.ac.uk/pride/archive) with the dataset
650 identifiers PXD051549 and PXD051551.

651

652 **Acknowledgements**

653 We thank B. Striepen, V. Carruthers, M.J. Gubbels and D. Soldati-Favre for the gift of antibodies or cell
654 lines. Mass spectrometry experiments were carried out using the facilities of the Montpellier
655 Proteomics Platform (PPM, MSPP site, BioCampus Montpellier), member of the Proteomics French
656 Infrastructure (ProFI). We also thank the developers and the managers of the VeupathDB.org and
657 ToxoDB.org databases, as well as scientists who contributed datasets. We acknowledge the MRI Cell
658 Imaging Facility, member of the national infrastructure France-BioImaging for image acquisitions and
659 cytometry analyses.

660

661 **Funding**

662 This work was supported by the Agence Nationale de la Recherche (grant ANR-22-CE20-0026 to S.B.
663 and F.V.).

664

665 **References**

666 1. Beinert H, Holm RH, Münck E. Iron-sulfur clusters: nature's modular, multipurpose structures.
667 Science. 1997;277: 653–659. doi:10.1126/science.277.5326.653

668 2. Andreini C, Putignano V, Rosato A, Banci L. The human iron-proteome. Metallomics. 2018;10:
669 1223–1231. doi:10.1039/c8mt00146d

670 3. Lill R, Freibert S-A. Mechanisms of mitochondrial iron-sulfur protein biogenesis. Annu Rev
671 Biochem. 2020;89: 471–499. doi:10.1146/annurev-biochem-013118-111540

672 4. Brzóska K, Meczyńska S, Kruszewski M. Iron-sulfur cluster proteins: electron transfer and
673 beyond. Acta Biochim Pol. 2006;53: 685–691.

674 5. Tsaousis AD. On the origin of Iron/Sulfur cluster biosynthesis in eukaryotes. Front Microbiol.
675 2019;10: 2478. doi:10.3389/fmicb.2019.02478

676 6. Garcia PS, D'Angelo F, Ollagnier De Choudens S, Dussouchaud M, Bouveret E, Gribaldo S, et al.
677 An early origin of iron–sulfur cluster biosynthesis machineries before Earth oxygenation. Nat
678 Ecol Evol. 2022;6: 1564–1572. doi:10.1038/s41559-022-01857-1

679 7. Braymer JJ, Freibert SA, Rakwalska-Bange M, Lill R. Mechanistic concepts of iron-sulfur protein
680 biogenesis in Biology. Biochimica et Biophysica Acta (BBA) - Molecular Cell Research.
681 2021;1868: 118863. doi:10.1016/j.bbamcr.2020.118863

682 8. Maio N, Rouault TA. Outlining the complex pathway of mammalian Fe-S cluster biogenesis.
683 Trends in Biochemical Sciences. 2020;45: 411–426. doi:10.1016/j.tibs.2020.02.001

684 9. Kispal G, Csere P, Prohl C, Lill R. The mitochondrial proteins Atm1p and Nfs1p are essential for
685 biogenesis of cytosolic Fe/S proteins. EMBO J. 1999;18: 3981–3989.
686 doi:10.1093/emboj/18.14.3981

687 10. Pondarré C, Antiochos BB, Campagna DR, Clarke SL, Greer EL, Deck KM, et al. The mitochondrial
688 ATP-binding cassette transporter Abcb7 is essential in mice and participates in cytosolic iron–
689 sulfur cluster biogenesis. Human Molecular Genetics. 2006;15: 953–964.
690 doi:10.1093/hmg/ddl012

691 11. Zuo J, Wu Z, Li Y, Shen Z, Feng X, Zhang M, et al. Mitochondrial ABC transporter ATM3 is
692 essential for cytosolic iron-sulfur cluster assembly. Plant Physiol. 2017;173: 2096–2109.
693 doi:10.1104/pp.16.01760

694 12. Camire EJ, Grossman JD, Thole GJ, Fleischman NM, Perlstein DL. The yeast Nbp35-Cfd1 cytosolic
695 iron-sulfur cluster scaffold is an ATPase. J Biol Chem. 2015;290: 23793–23802.
696 doi:10.1074/jbc.M115.667022

697 13. Netz DJA, Stümpfig M, Doré C, Mühlenhoff U, Pierik AJ, Lill R. Tah18 transfers electrons to Dre2
698 in cytosolic iron-sulfur protein biogenesis. Nat Chem Biol. 2010;6: 758–765.
699 doi:10.1038/nchembio.432

700 14. Kohbushi H, Nakai Y, Kikuchi S, Yabe T, Hori H, Nakai M. Arabidopsis cytosolic Nbp35
701 homodimer can assemble both [2Fe–2S] and [4Fe–4S] clusters in two distinct domains.
702 Biochemical and Biophysical Research Communications. 2009;378: 810–815.
703 doi:10.1016/j.bbrc.2008.11.138

704 15. Balk J, Pierik AJ, Netz DJA, Mühlenhoff U, Lill R. The hydrogenase-like Nar1p is essential for
705 maturation of cytosolic and nuclear iron-sulphur proteins. EMBO J. 2004;23: 2105–2115.
706 doi:10.1038/sj.emboj.7600216

707 16. Kassube SA, Thomä NH. Structural insights into Fe–S protein biogenesis by the CIA targeting
708 complex. Nat Struct Mol Biol. 2020;27: 735–742. doi:10.1038/s41594-020-0454-0

709 17. Sanchez SG, Besteiro S. The pathogenicity and virulence of Toxoplasma gondii. Virulence.
710 2021;12: 3095–3114. doi:10.1080/21505594.2021.2012346

711 18. Sheiner L, Vaidya AB, McFadden GI. The metabolic roles of the endosymbiotic organelles of
712 Toxoplasma and Plasmodium spp. Curr Opin Microbiol. 2013;16: 452–458.
713 doi:10.1016/j.mib.2013.07.003

714 19. Pamukcu S, Cerutti A, Bordat Y, Hem S, Rofidal V, Besteiro S. Differential contribution of two
715 organelles of endosymbiotic origin to iron-sulfur cluster synthesis and overall fitness in
716 Toxoplasma. Soldati-Favre D, editor. PLoS Pathog. 2021;17: e1010096.
717 doi:10.1371/journal.ppat.1010096

718 20. Aw YTV, Seidi A, Hayward JA, Lee J, Victor Makota F, Rug M, et al. A key cytosolic iron-sulfur
719 cluster synthesis protein localises to the mitochondrion of Toxoplasma gondii. Mol Microbiol.
720 2020; mmi.14651. doi:10.1111/mmi.14651

721 21. Renaud EA, Pamukcu S, Cerutti A, Berry L, Lemaire-Vieille C, Yamaryo-Botté Y, et al. Disrupting
722 the plastidic iron-sulfur cluster biogenesis pathway in Toxoplasma gondii has pleiotropic effects
723 irreversibly impacting parasite viability. J Biol Chem. 2022;298: 102243.
724 doi:10.1016/j.jbc.2022.102243

725 22. Tsaousis AD, Gentekaki E, Eme L, Gaston D, Roger AJ. Evolution of the cytosolic iron-sulfur
726 cluster assembly machinery in Blastocystis species and other microbial eukaryotes. Eukaryot
727 Cell. 2014;13: 143–153. doi:10.1128/EC.00158-13

728 23. Pyrih J, Žárský V, Fellows JD, Grosche C, Wloga D, Striepen B, et al. The iron-sulfur scaffold
729 protein HCF101 unveils the complexity of organellar evolution in SAR, Haptista and Cryptista.
730 BMC Ecol Evol. 2021;21: 46. doi:10.1186/s12862-021-01777-x

731 24. Lezhneva L, Amann K, Meurer J. The universally conserved HCF101 protein is involved in
732 assembly of [4Fe-4S]-cluster-containing complexes in *Arabidopsis thaliana* chloroplasts. The
733 Plant Journal. 2004;37: 174–185. doi:10.1046/j.1365-313X.2003.01952.x

734 25. Schwenkert S, Netz DJA, Frazzon J, Pierik AJ, Bill E, Gross J, et al. Chloroplast HCF101 is a
735 scaffold protein for [4Fe-4S] cluster assembly. Biochem J. 2009;425: 207–214.
736 doi:10.1042/BJ20091290

737 26. Leipe DD, Wolf YI, Koonin EV, Aravind L. Classification and evolution of P-loop GTPases and
738 related ATPases. Journal of Molecular Biology. 2002;317: 41–72. doi:10.1006/jmbi.2001.5378

739 27. Boyd JM, Drevland RM, Downs DM, Graham DE. Archaeal ApbC/Nbp35 homologs function as
740 iron-sulfur cluster carrier proteins. J Bacteriol. 2009;191: 1490–1497. doi:10.1128/JB.01469-08

741 28. Mashruwala AA, Boyd JM. Investigating the role(s) of SufT and the domain of unknown function
742 59 (DUF59) in the maturation of iron–sulfur proteins. Curr Genet. 2018;64: 9–16.
743 doi:10.1007/s00294-017-0716-5

744 29. Meurer J, Meierhoff K, Westhoff P. Isolation of high-chlorophyll-fluorescence mutants
745 ofArabidopsis thaliana and their characterisation by spectroscopy, immunoblotting and
746 Northern hybridisation. Planta. 1996;198: 385–396. doi:10.1007/BF00620055

747 30. Mathur V, Salomaki ED, Wakeman KC, Na I, Kwong WK, Kolisko M, et al. Reconstruction of
748 plastid proteomes of apicomplexans and close relatives reveals the major evolutionary
749 outcomes of cryptic plastids. Mol Biol Evol. 2023;40: msad002. doi:10.1093/molbev/msad002

750 31. Zhu G, Marchewka MJ, Keithly JS. Cryptosporidium parvum appears to lack a plastid genome.
751 Microbiology. 2000;146: 315–321. doi:10.1099/00221287-146-2-315

752 32. Moore RB, Oborník M, Janouskovec J, Chrudimský T, Vancová M, Green DH, et al. A
753 photosynthetic alveolate closely related to apicomplexan parasites. Nature. 2008;451: 959–
754 963. doi:10.1038/nature06635

755 33. Marquez MD, Greth C, Buzuk A, Liu Y, Blinn CM, Beller S, et al. Cytosolic iron–sulfur protein
756 assembly system identifies clients by a C-terminal tripeptide. Proc Natl Acad Sci USA. 2023;120:
757 e2311057120. doi:10.1073/pnas.2311057120

758 34. Meissner M, Brecht S, Bujard H, Soldati D. Modulation of myosin A expression by a newly
759 established tetracycline repressor-based inducible system in Toxoplasma gondii. Nucleic Acids
760 Res. 2001;29: E115.

761 35. Cerutti A, Blanchard N, Besteiro S. The bradyzoite: a key developmental stage for the
762 persistence and pathogenesis of toxoplasmosis. Pathogens. 2020;9: 234.
763 doi:10.3390/pathogens9030234

764 36. Gubbels M-J, Wieffer M, Striepen B. Fluorescent protein tagging in Toxoplasma gondii:
765 identification of a novel inner membrane complex component conserved among Apicomplexa.
766 Molecular and Biochemical Parasitology. 2004;137: 99–110.
767 doi:10.1016/j.molbiopara.2004.05.007

768 37. Francia ME, Striepen B. Cell division in apicomplexan parasites. Nat Rev Microbiol. 2014;12:
769 125–136. doi:10.1038/nrmicro3184

770 38. Nolan SJ, Romano JD, Kline JT, Coppens I. Novel approaches to kill Toxoplasma gondii by
771 exploiting the uncontrolled uptake of unsaturated fatty acids and vulnerability to lipid storage
772 inhibition of the parasite. Antimicrob Agents Chemother. 2018;62: e00347-18.
773 doi:10.1128/AAC.00347-18

774 39. Jarc E, Petan T. Lipid droplets and the management of cellular stress. Yale J Biol Med. 2019;92:
775 435–452.

776 40. Nadipuram SM, Thind AC, Rayatpisheh S, Wohlschlegel JA, Bradley PJ. Proximity biotinylation
777 reveals novel secreted dense granule proteins of Toxoplasma gondii bradyzoites. PLoS One.
778 2020;15: e0232552. doi:10.1371/journal.pone.0232552

779 41. Jung C, Lee CY-F, Grigg ME. The SRS superfamily of Toxoplasma surface proteins. International
780 Journal for Parasitology. 2004;34: 285–296. doi:10.1016/j.ijpara.2003.12.004

781 42. Tomita T, Bzik DJ, Ma YF, Fox BA, Markillie LM, Taylor RC, et al. The Toxoplasma gondii cyst wall
782 protein CST1 is critical for cyst wall integrity and promotes bradyzoite persistence. PLoS Pathog.
783 2013;9: e1003823. doi:10.1371/journal.ppat.1003823

784 43. Ben Chaabene R, Lentini G, Soldati-Favre D. Biogenesis and discharge of the rhoptries: Key
785 organelles for entry and hijack of host cells by the Apicomplexa. Mol Microbiol. 2021;115: 453–
786 465. doi:10.1111/mmi.14674

787 44. Mueller C, Klages N, Jacot D, Santos JM, Cabrera A, Gilberger TW, et al. The Toxoplasma protein
788 ARO mediates the apical positioning of rhoptry organelles, a prerequisite for host cell invasion.
789 Cell Host & Microbe. 2013;13: 289–301. doi:10.1016/j.chom.2013.02.001

790 45. Valasatava Y, Rosato A, Banci L, Andreini C. MetalPredator: a web server to predict iron-sulfur
791 cluster binding proteomes. Bioinformatics. 2016;32: 2850–2852.
792 doi:10.1093/bioinformatics/btw238

793 46. Barylyuk K, Koreny L, Ke H, Butterworth S, Crook OM, Lassadi I, et al. A comprehensive
794 subcellular atlas of the Toxoplasma proteome via hyperLOPIT provides spatial context for
795 protein functions. Cell Host & Microbe. 2020; S193131282030514X.
796 doi:10.1016/j.chom.2020.09.011

797 47. Stehling O, Mascarenhas J, Vashisht AA, Sheftel AD, Niggemeyer B, Rösser R, et al. Human
798 CIA2A-FAM96A and CIA2B-FAM96B integrate iron homeostasis and maturation of different
799 Subsets of cytosolic-nuclear iron-sulfur proteins. Cell Metabolism. 2013;18: 187–198.
800 doi:10.1016/j.cmet.2013.06.015

801 48. Schmidt EK, Clavarino G, Ceppi M, Pierre P. SUnSET, a nonradioactive method to monitor
802 protein synthesis. Nat Methods. 2009;6: 275–277. doi:10.1038/nmeth.1314

803 49. Bych K, Kerscher S, Netz DJA, Pierik AJ, Zwicker K, Huynen MA, et al. The iron–sulphur protein
804 Ind1 is required for effective complex I assembly. EMBO J. 2008;27: 1736–1746.
805 doi:10.1038/emboj.2008.98

806 50. Aubert C, Mandin P, Py B. Mrp and SufT, two bacterial homologs of eukaryotic CIA Factors
807 involved in Fe-S clusters biogenesis. Inorganics. 2023;11: 431. doi:10.3390/inorganics11110431

808 51. Stehling O, Jeoung J-H, Freibert SA, Paul VD, Bänfer S, Niggemeyer B, et al. Function and crystal
809 structure of the dimeric P-loop ATPase CFD1 coordinating an exposed [4Fe-4S] cluster for
810 transfer to apoproteins. Proc Natl Acad Sci U S A. 2018;115: E9085–E9094.
811 doi:10.1073/pnas.1807762115

812 52. Mashruwala AA, Bhatt S, Poudel S, Boyd ES, Boyd JM. The DUF59 containing protein SufT is
813 involved in the maturation of Iron-Sulfur (FeS) proteins during conditions of high FeS cofactor
814 demand in Staphylococcus aureus. PLoS Genet. 2016;12: e1006233.
815 doi:10.1371/journal.pgen.1006233

816 53. Maclean AE, Sloan MA, Renaud EA, Demolombe V, Besteiro S, Sheiner L. The Toxoplasma gondii
817 mitochondrial transporter ABCB7 is essential for cytosolic iron-sulfur cluster biogenesis and
818 protein translation. 2024. doi:10.1101/2024.03.15.585200

819 54. Sidik SM, Huet D, Ganesan SM, Huynh M-H, Wang T, Nasamu AS, et al. A Genome-wide CRISPR
820 Screen in Toxoplasma Identifies Essential Apicomplexan Genes. Cell. 2016;166: 1423-1435.e12.
821 doi:10.1016/j.cell.2016.08.019

822 55. Liang D, Minikes AM, Jiang X. Ferroptosis at the intersection of lipid metabolism and cellular
823 signaling. Molecular Cell. 2022;82: 2215–2227. doi:10.1016/j.molcel.2022.03.022

824 56. Renaud EA, Maupin AJM, Bordat Y, Graindorge A, Berry L, Besteiro S. Iron depletion has
825 different consequences on the growth and survival of Toxoplasma gondii strains. Virulence.
826 2024;15: 2329566. doi:10.1080/21505594.2024.2329566

827 57. Paul VD, Mühlenhoff U, Stümpfig M, Seebacher J, Kugler KG, Renicke C, et al. The deca-GX3
828 proteins Yae1-Lto1 function as adaptors recruiting the ABC protein Rli1 for iron-sulfur cluster
829 insertion. eLife. 2015;4: e08231. doi:10.7554/eLife.08231

830 58. Zhai C, Li Y, Mascarenhas C, Lin Q, Li K, Vyrides I, et al. The function of ORAOV1/LTO1, a gene
831 that is overexpressed frequently in cancer: essential roles in the function and biogenesis of the
832 ribosome. Oncogene. 2014;33: 484–494. doi:10.1038/onc.2012.604

833 59. Prusty NR, Camponeschi F, Ciofi-Baffoni S, Banci L. The human YAE1-ORAOV1 complex of the
834 cytosolic iron-sulfur protein assembly machinery binds a [4Fe-4S] cluster. Inorganica Chimica
835 Acta. 2021;518: 120252. doi:10.1016/j.ica.2021.120252

836 60. Navarro-Quiles C, Mateo-Bonmatí E, Micol JL. ABCE Proteins: From Molecules to development.
837 Front Plant Sci. 2018;9: 1125. doi:10.3389/fpls.2018.01125

838 61. Sheiner L, Demerly JL, Poulsen N, Beatty WL, Lucas O, Behnke MS, et al. A Systematic Screen to
839 Discover and Analyze Apicoplast Proteins Identifies a Conserved and Essential Protein Import
840 Factor. PLoS Pathog. 2011;7. doi:10.1371/journal.ppat.1002392

841 62. Grosche C, Diehl A, Rensing SA, Maier UG. Iron–sulfur cluster biosynthesis in algae with
842 complex plastids. Embley M, editor. Genome Biology and Evolution. 2018;10: 2061–2071.
843 doi:10.1093/gbe/evy156

844 63. Lévêque MF, Berry L, Cipriano MJ, Nguyen H-M, Striepen B, Besteiro S. Autophagy-related
845 protein ATG8 has a noncanonical function for apicoplast inheritance in Toxoplasma gondii.
846 MBio. 2015;6: e01446-15.

847 64. Anderson-White BR, Ivey FD, Cheng K, Szatanek T, Lorestani A, Beckers CJ, et al. A family of
848 intermediate filament-like proteins is sequentially assembled into the cytoskeleton of
849 Toxoplasma gondii. Cell Microbiol. 2011;13: 18–31. doi:10.1111/j.1462-5822.2010.01514.x

850 65. Couvreur G, Sadak A, Fortier B, Dubremetz JF. Surface antigens of Toxoplasma gondii.
851 Parasitology. 1988;97 (Pt 1): 1–10.

852 66. Herm-Gotz A. Toxoplasma gondii myosin A and its light chain: a fast, single-headed, plus-end-
853 directed motor. The EMBO Journal. 2002;21: 2149–2158. doi:10.1093/emboj/21.9.2149

854 67. Hajj HE, Lebrun M, Fourmaux MN, Vial H, Dubremetz JF. Characterization, biosynthesis and fate
855 of ROP7, a ROP2 related rhoptry protein of Toxoplasma gondii☆. Molecular and Biochemical
856 Parasitology. 2006;146: 98–100. doi:10.1016/j.molbiopara.2005.10.011

857 68. Berger N, Vignols F, Przybyla-Toscano J, Roland M, Rofidal V, Touraine B, et al. Identification of
858 client iron–sulfur proteins of the chloroplastic NFU2 transfer protein in Arabidopsis thaliana.
859 Takahashi H, editor. Journal of Experimental Botany. 2020;71: 4171–4187.
860 doi:10.1093/jxb/eraa166

861 69. Cox J, Mann M. MaxQuant enables high peptide identification rates, individualized p.p.b.-range
862 mass accuracies and proteome-wide protein quantification. Nat Biotechnol. 2008;26: 1367–
863 1372. doi:10.1038/nbt.1511

864 70. Hehl AB, Basso WU, Lippuner C, Ramakrishnan C, Okoniewski M, Walker RA, et al. Asexual
865 expansion of Toxoplasma gondii merozoites is distinct from tachyzoites and entails expression
866 of non-overlapping gene families to attach, invade, and replicate within feline enterocytes.
867 BMC Genomics. 2015;16: 66. doi:10.1186/s12864-015-1225-x

868 71. Smyth GK. Linear models and empirical bayes methods for assessing differential expression in
869 microarray experiments. Stat Appl Genet Mol Biol. 2004;3: Article3. doi:10.2202/1544-
870 6115.1027

871 72. Daniel Gietz R, Woods RA. Transformation of yeast by lithium acetate/single-stranded carrier
872 DNA/polyethylene glycol method. Methods in Enzymology. Elsevier; 2002. pp. 87–96.
873 doi:10.1016/S0076-6879(02)50957-5

874 73. Semenovskaya K, Lévêque MF, Berry L, Bordat Y, Dubremetz J, Lebrun M, et al. TgZFP2 is a
875 novel zinc finger protein involved in coordinating mitosis and budding in Toxoplasma. Cellular
876 Microbiology. 2020;22: e13120.

877 74. Henkel S, Frohnecke N, Maus D, McConville MJ, Laue M, Blume M, et al. Toxoplasma gondii
878 apicoplast-resident ferredoxin is an essential electron transfer protein for the MEP isoprenoid-
879 biosynthetic pathway. J Biol Chem. 2022;298: 101468. doi:10.1016/j.jbc.2021.101468

880 75. Lamarque MH, Roques M, Kong-Hap M, Tonkin ML, Rugarabamu G, Marq J-B, et al. Plasticity
881 and redundancy among AMA-RON pairs ensure host cell entry of Toxoplasma parasites. Nat
882 Commun. 2014;5: 4098. doi:10.1038/ncomms5098

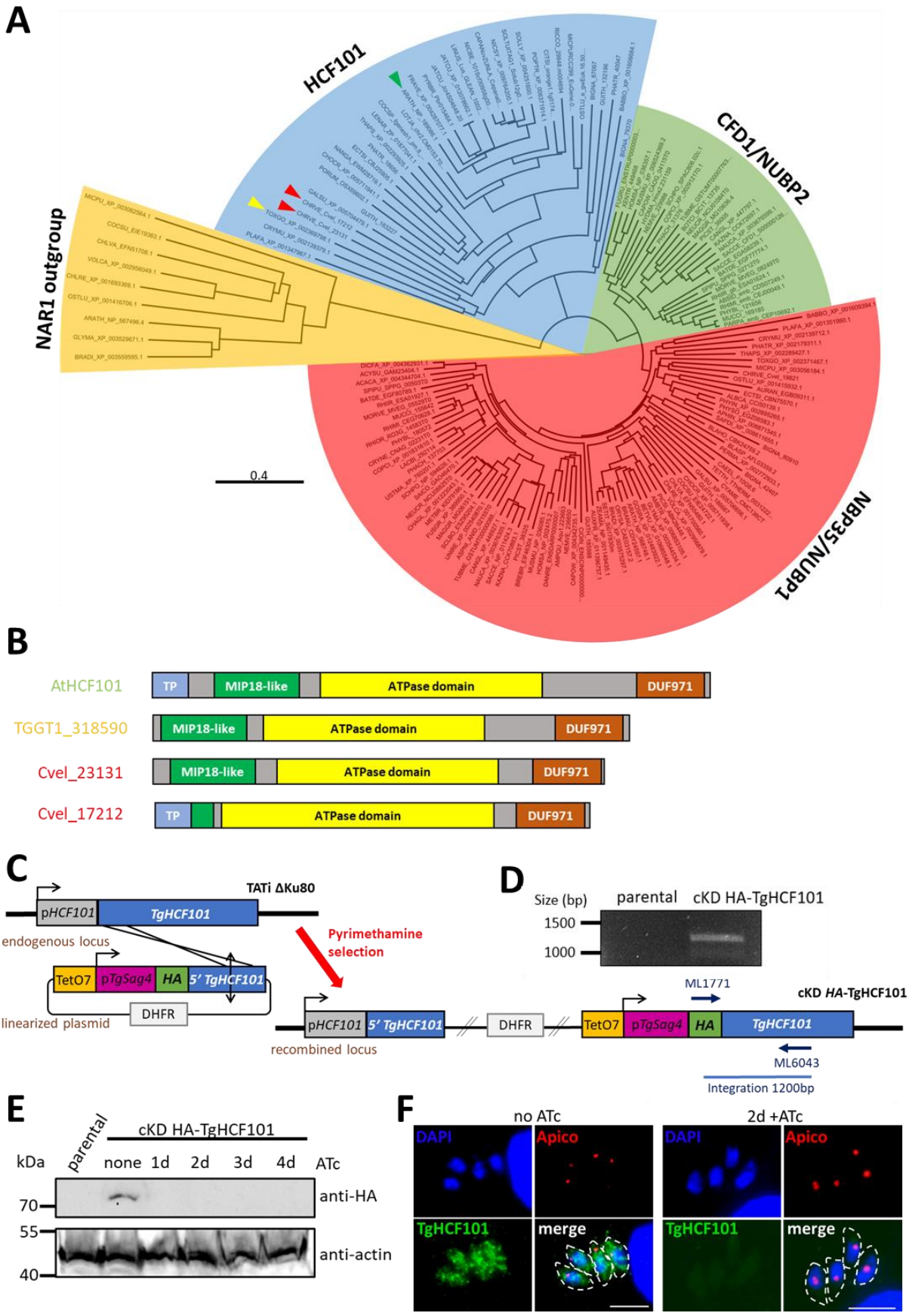

883

884 **Figure 1. TgHCF101 is a cytosolic protein. A.** Evolutionary relationship of proteins of the MRP family.
885 Eukaryotic sequences from HCF101 homologs were aligned and submitted phylogenetic analysis with

886 the unweighted paired group mean arithmetic method. Scale bar represents 0.4 residue substitution
887 per site. NAR1 is used as an outgroup. The plant HCF101 homolog from *A. thaliana* is indicated by a
888 green arrowhead, TgHCF101 by a yellow arrowhead and the two homologs present in *C. velia* are
889 indicated by red arrowheads. **B.** Schematic representation of HCF101 homologs in *A. thaliana*
890 (AtHCF101), in *T. gondii* (TGGT1_318590) and in *C. velia* (Cvel_23131, Cvel_17212). Main domains are
891 highlighted on the sequences; TP: Transit peptide, MIP18-like domain (or Domain of unknown function
892 59, DUF59), the ATPase domain and DUF971. **C.** Strategy for generating the inducible knockdown of
893 *TgHCF101* by promoter replacement and simultaneous N-terminal tagging of the TgHCF101 protein in
894 the TATi ΔKu80 cell line. **D.** Diagnostic PCR for checking correct integration of using the primers
895 mentioned in (B), on genomic DNAs of a transgenic parasite clone and of the parental strain. **E.**
896 Immunoblot analysis of the cKD-TgHCF101 mutant and parental line showing efficient tagging and
897 downregulation of TgHCF101 starting at 24h of treatment with ATc. Actin was used as a loading control.
898 **F.** Immunofluorescence assay showing a cytosolic signal for TgHCF101 protein (labeled with an anti-
899 HA), with no particular co-localization with the apicoplast (Apico, labeled with anti-PDH-E2), and total
900 depletion of the protein after 48h of ATc treatment. DNA was stained with 4',6-diamidino-2-
901 phenylindole (DAPI). Scale bar= 5 µm.

902

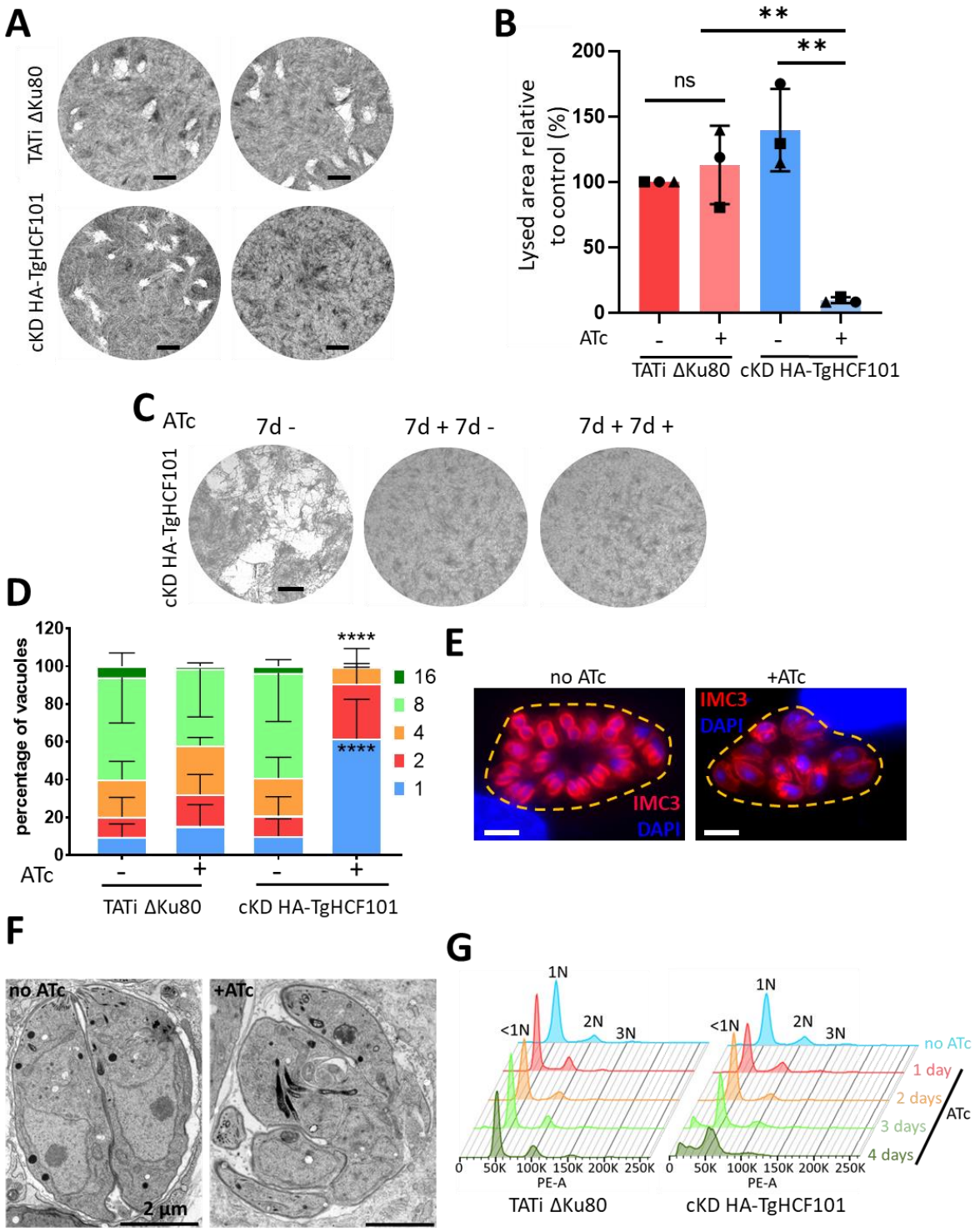

Figure 2. TgHCF101 is essential for parasite growth and survival. A. Plaque assays were carried out by infecting a monolayer of HFFs with TATi ΔKu80 or cKD-TgHCF101 cell lines for 7 days in the presence or absence of ATc. Scale bar= 2 mm. **B.** Quantification of plaque area observed in (A). Results are expressed as percentage of lysed area relative to control (TATi ΔKu80 -ATc, set as 100% for reference). Values represented are mean ± SD from n=3 independent biological replicates, ** p-value ≤ 0.01, Student *t*-test **C.** Plaque assays were carried out with cKD-TgHCF101 parasites as described in (A) but for the '7d+7d-' condition, ATc was washed-out after 7 days and parasites were allowed to grow for another 7 days without ATc, while in the '7d+7d+' condition, ATc treatment was maintained for 7 more days. The '7d –' control was kept without ATc for 7 days of growth. Scale bar= 2mm. **D.** Replication

913 assay of parental (TATi ΔKu80) and transgenic cell lines (cKD-TgHCF101): parasites were pre-cultured
914 for 48h in the presence or absence of ATc and allowed to invade HFF-coated coverslips for another 24h
915 in the presence or absence of ATc, for a total of up to 72h of treatment with ATc. Number of parasites
916 per vacuole was quantified for each condition and expressed as a percentage, 200 vacuoles were
917 counted for each condition. Values represented are mean ± SD of 3 independent biological replicates,
918 **** p-value ≤ 0.0001 by two-way ANOVA with Dunnett's multiple comparison test, showing a
919 significant difference when comparing the TATi ΔKu80 control and cKD-TgHCF101+ATc parasites for
920 percentage of vacuoles containing 1 or 8 parasites. **E.** DNA content analysis by flow cytometry on TATi
921 ΔKu80 and cKD-TgHCF101 parasites treated or not with ATc up to 4 days and stained with propidium
922 iodide. 1N, 2N, 3N represents the ploïdy with <1N correspond to parasite with less than 1 full nuclear
923 DNA content. **F.** Immunofluorescence assay of cKD-TgHCF101 parasites showing asynchronous division
924 of parasites growing in the same vacuole (outlined with a yellow dotted line) upon TgHCF101 depletion
925 (+ATc condition: parasites pre-incubated for 48h with ATc and allowed to invade coverslips for another
926 36h in the presence of ATc). Individual parasites and budding daughter cells are outlined by anti-IMC3
927 antibody staining (magenta), DNA was stained with DAPI. Scale bar= 5 µm. **G.** Electron microscopy of
928 cKD-TgHCF101 parasites pre-incubated with ATc for 24h before being released from their host cell and
929 allowed to reinvade for 24h in the presence (+ATc) or grown in absence of ATc (-ATc). Scale bar= 2 µm.

930

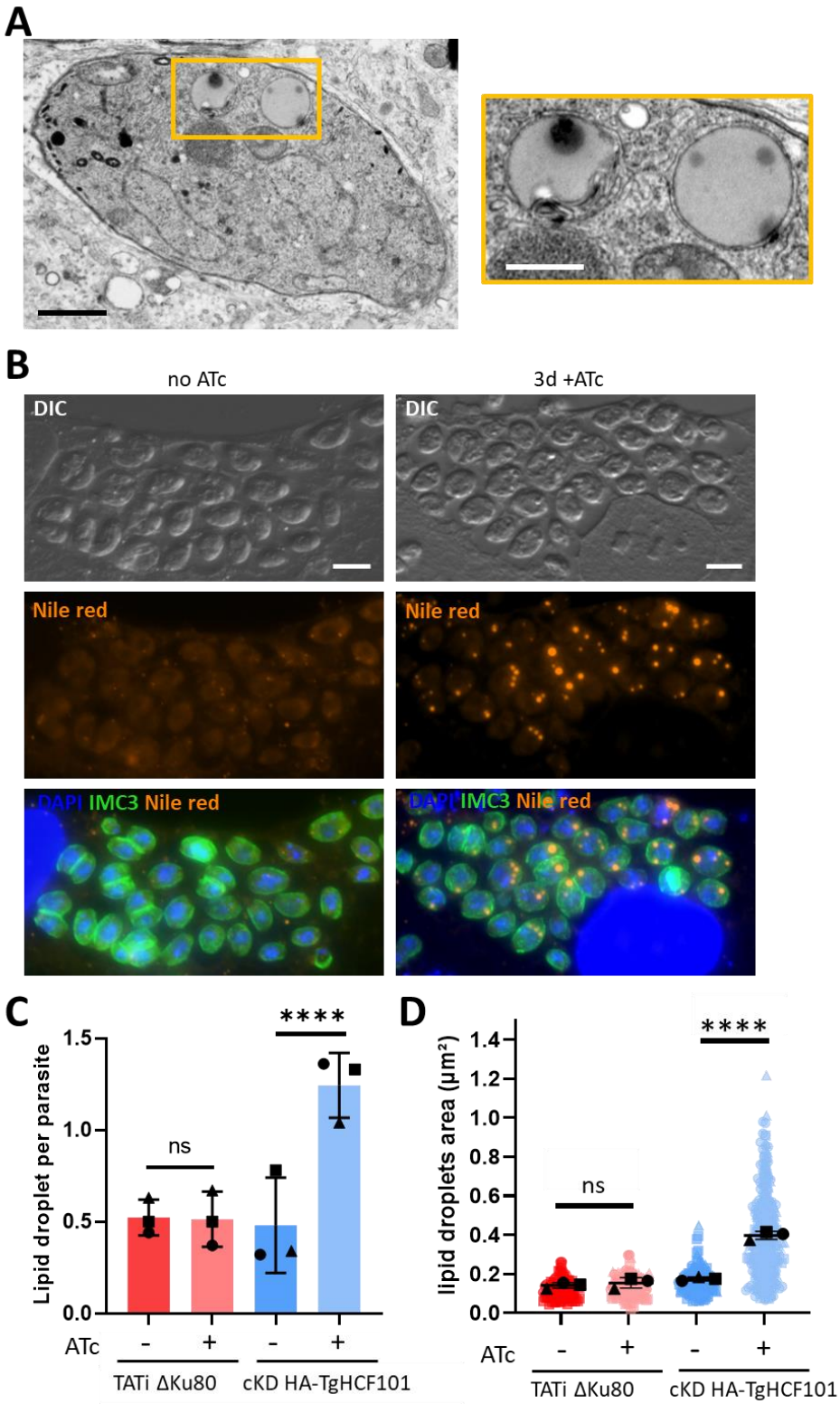

Figure 3. TgHCF101 depletion induces lipid droplet accumulation. A. Electron microscopy of cKD-TgHCF101 parasites pre-incubated with ATc for 48h and allowed to reinvade for 24h in the presence of ATc. Scale bar= 1 µm. The panel on the right corresponds to a magnification of the selection on the left panel, highlighting lipid droplets. Scale bar= 500 nm **B.** Fluorescent imaging of parasites from the cKD-TgHCF101 cell line treated for 72h with ATc or in grown the absence of ATc, shows an accumulation of lipid droplet upon TgHCF101 depletion. Lipid droplets were detected with Nile red

938 (orange), parasites are outlined with an anti-IMC3 antibody (green) and DNA is stained with DAPI. DIC=
939 Differential interference contrast. Scale bar= 5 µm. **C.** and **D.** correspond to the quantification of lipid
940 droplet number and area, respectively. 100 parasites were analyzed per condition. the parental (TATi
941 ΔKu80) and transgenic (cKD-TgHCF101) parasites were grown in absence of ATc, or in presence of ATc
942 for 72h. Values are represented as the mean ± SD of n=3 independent biological replicates; ns, not
943 significant (p-value>0.05), **** p-value ≤ 0.0001, Student's *t*-test.

944

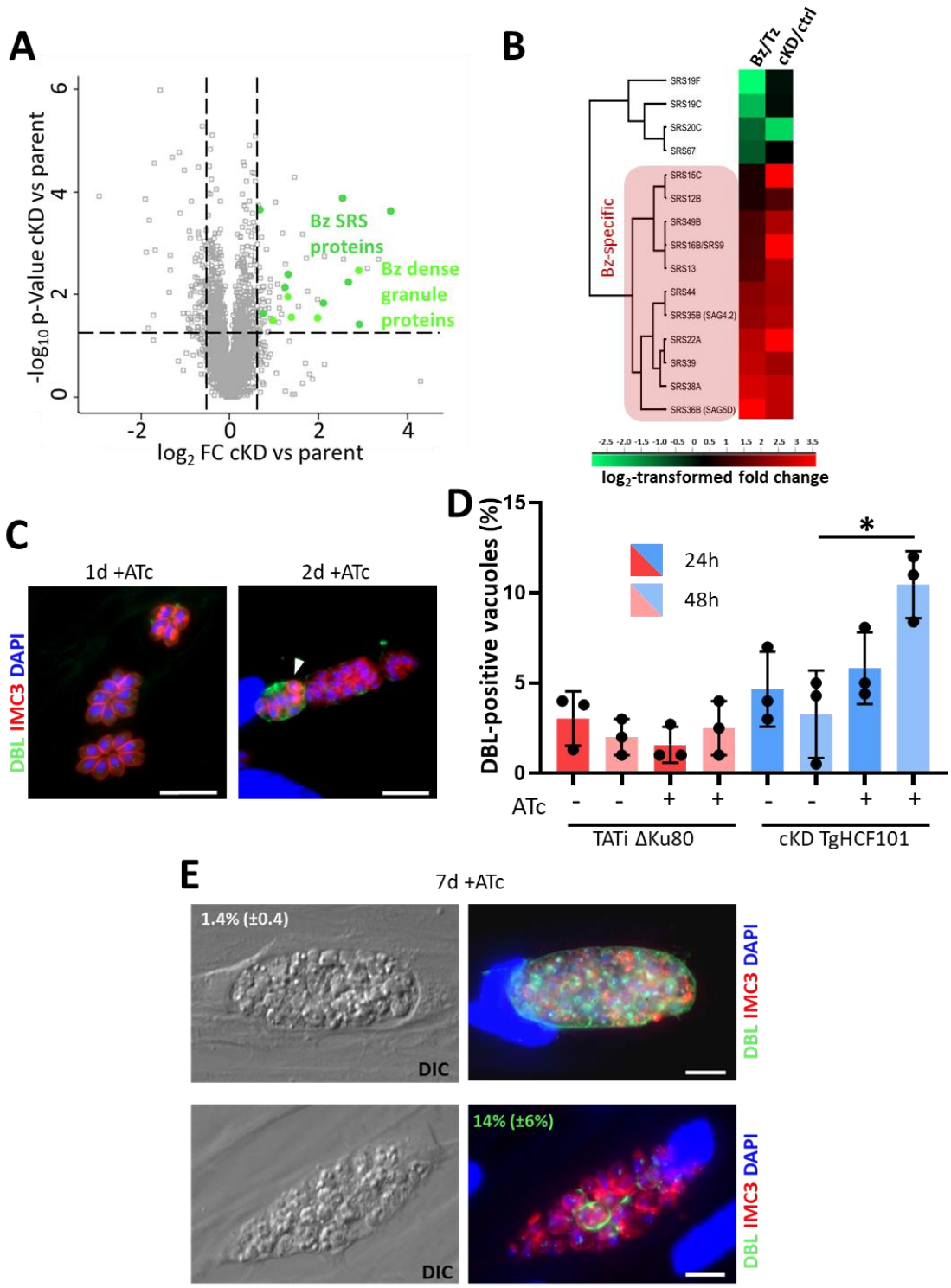

Figure 4. TgHCF101-depleted parasites express bradyzoite-specific markers but are unable to complete their conversion. A. Volcano plot showing differential expression of proteins impacted by TgHCF101 depletion after 72h of ATc treatment analyzed by label free quantitative proteomic. X-axis corresponds to the $\log_2$ of the fold-change (FC) and the Y-axis corresponds to the $-\log_{10}$ of the p-value, when comparing cKD-TgHCF101 expression values to the TATi ΔKu80 parental cell line. Statistical analyses were performed with ANOVA on 4 independent biological replicates. Cut-offs were set at ≤1.5- or ≥1.5-FC and p-value ≤0.05. Significant hits corresponding to stage-specific protein are highlighted in green on the graph. **B.** Clustering of bradyzoite (Bz) or tachyzoite (Tz)-specific proteins

954 of the SRS family shows specific enrichment of bradyzoite proteins upon TgHCF101 depletion. **C.**
955 Immunofluorescence assay of cKD-TgHCF101 treated for 24h or 48h with ATc, cyst wall is labelled with
956 DBL, parasites periphery is outlined with anti-IMC3 antibody and DNA is stained with DAPI. Scale bar=
957 10µm **D.** Corresponds to the quantification of the percentage of vacuoles presenting a DBL positive
958 signal as shown in (C). Values are represented as the mean ± SD of n=3 independent biological
959 replicates, * p-value ≤ 0.05, Student's *t*-test. **E.** Immunofluorescence assay of cKD-TgHCF101 treated
960 for 7 days in the presence of ATc, cyst wall is labelled with DBL, parasites are outlined with anti-IMC3
961 antibody and DNA is stained with DAPI. The percentage of DBL positive vacuoles of corresponding size
962 (more than 2 parasites per vacuole, top; or 2 parasites per vacuole or less, bottom) is specified as mean
963 ± SD of n=3 independent biological replicates. DIC= Differential interference contrast. Scale bar= 10
964 µm.

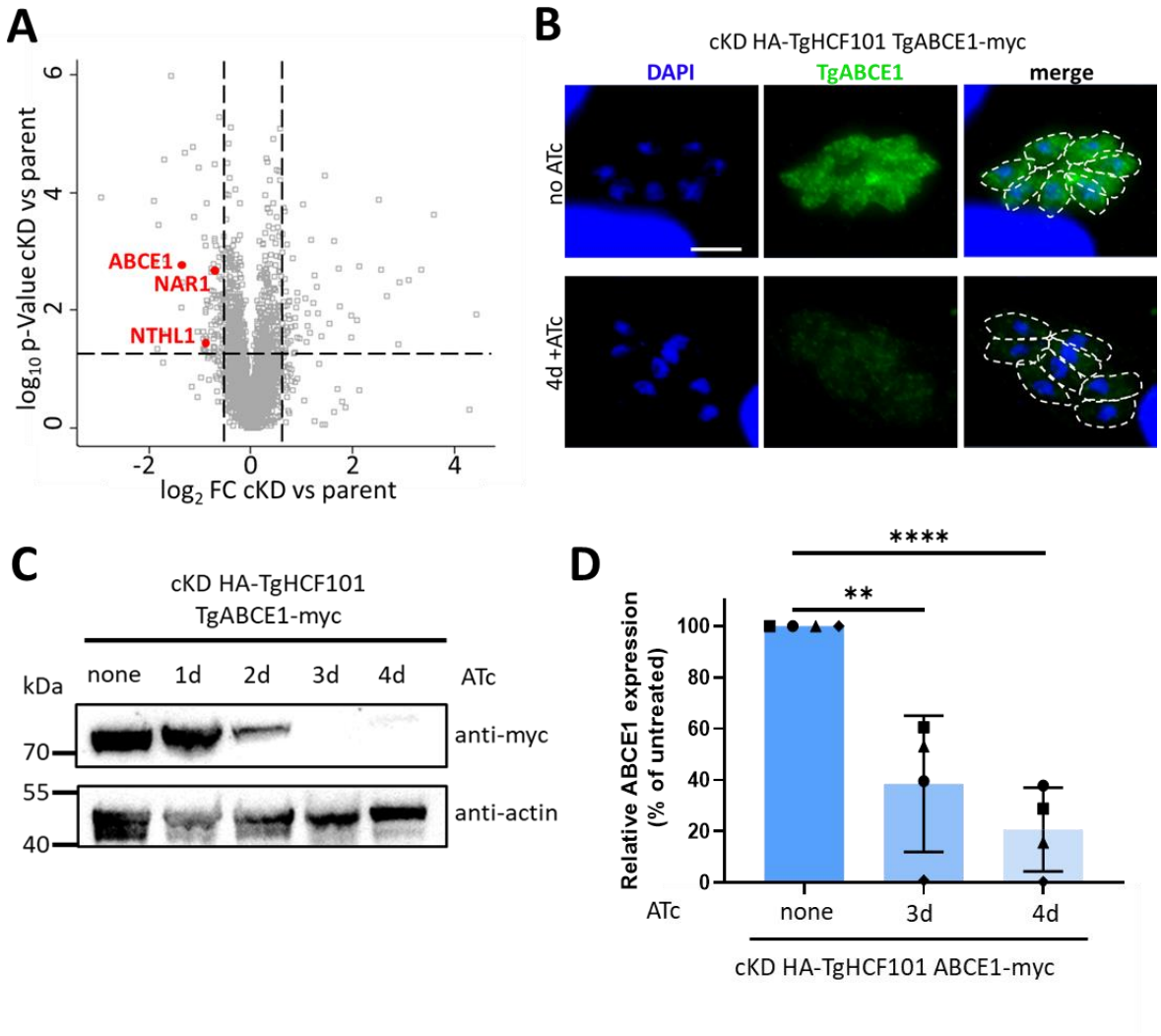

Figure 5. TgHCF101 is involved in Fe-S cluster biogenesis of the CIA pathway. A. Volcano plot showing differential expression of proteins impacted by TgHCF101 depletion after 72h of ATc treatment analyzed by label free quantitative proteomic. Cut-offs were set at ≤1.5- or ≥1.5-fold change (FC) and p-value ≤0.05. Significant hits corresponding to predicted Fe-S cluster proteins are highlighted in red on the graph. **B.** Immunofluorescence assay for the detection of the myc-tagged protein TgABCE1 in the cKD TgHCF101 genetic background. Parasites were pre-incubated for 48h in the presence of ATc and allowed to invade HFF coated coverslips for another 48h in the presence of ATc. The control (no ATc) was infected 24h prior to fixation. TgABCE1 was detected with anti-myc antibody and DNA was stained with DAPI. Parasites periphery is outlined by white dotted lines. Scale bar=5 µm. **C.** Immunoblot analysis of TgABCE1 expression shows decrease upon TgHCF101 depletion up to 4 days of treatment with ATc in the cKD HA-TgHCF101 TgABCE1-myc cell line. TgABCE1 expression was detected with anti-myc antibody and anti-actin antibody was used as a loading control. **D.** Decrease of TgABCE1 expression upon TgHCF101 depletion was quantified by band densitometry analysis and normalized on the loading control of each respective lane. The relative abundance of ABCE1 is presented as a percentage relative to the untreated control, set as 100%, for each biological replicate. Values are represented as the mean ± SD from n=4 independent biological replicates, ** p-value ≤ 0.01, **** p-value ≤ 0.0001, Student's *t*-test.

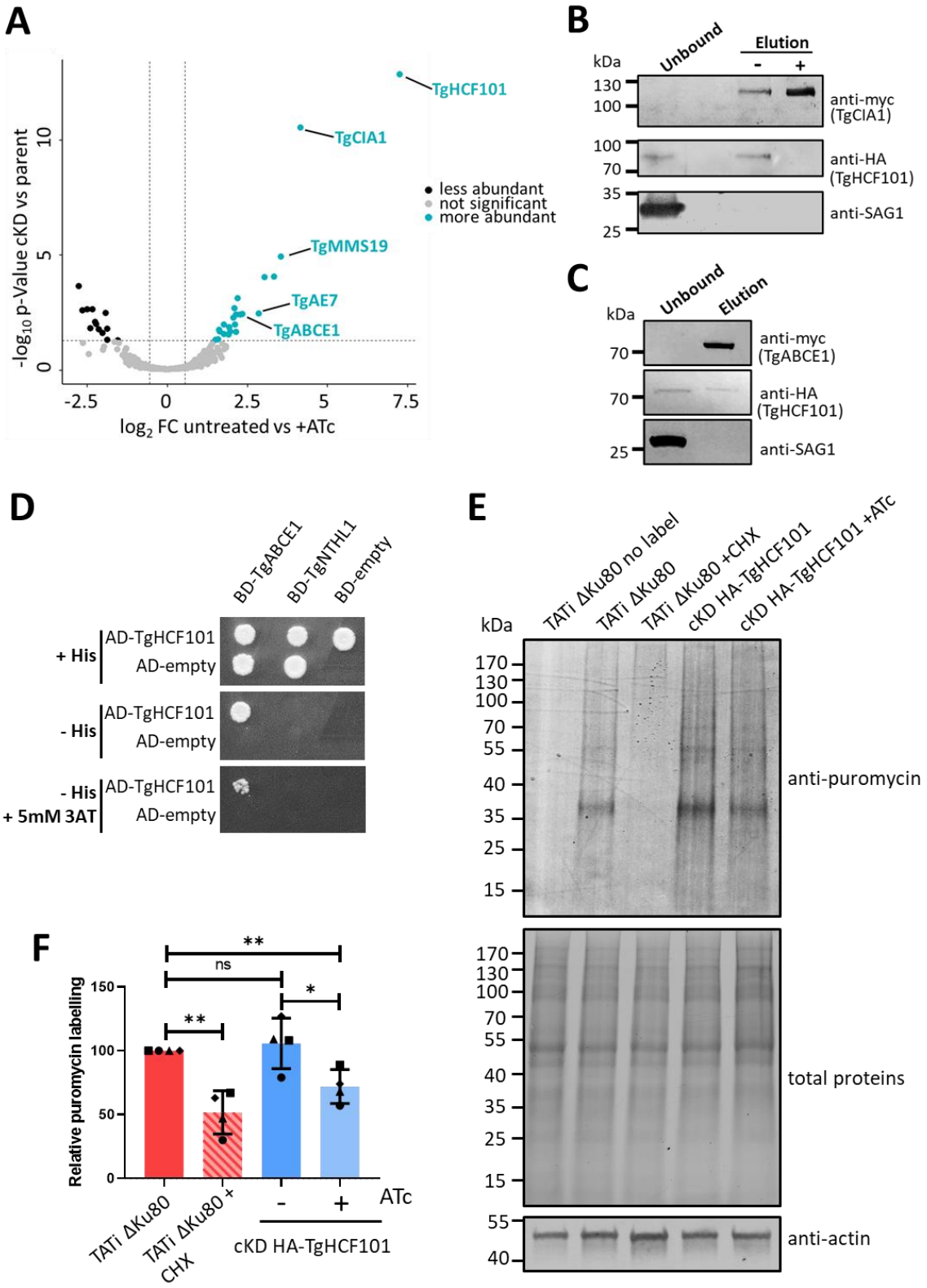

Figure 6. TGHCF101 is associated to the CIA targeting complex and specifically interacts with TgABCE1. A. Volcano plot showing differential expression of TgHCF101 and co-immunoprecipitated proteins in the cKD HA-TgHCF101 cell line after TgHCF101 depletion (with 72h of ATc treatment) or not, as analyzed by quantitative proteomic. Cut-offs were set at ≤1.5- or ≥1.5-fold change and p-value ≤0.05. Upregulated proteins are highlighted in blue, significant hits corresponding to predicted

990 proteins of the CIA targeting complex and target protein TgABCE1 were annotated on the graph. **B.**
991 Immunoblot analysis of a reverse co-immunoprecipitation assay of the myc-tagged TgCIA1 protein in
992 the cKD HA-TgHCF101 background shows specific co-immunoprecipitation of TgHCF101, which is
993 absent upon depletion by ATc. The anti-SAG1 antibody was used as a control for unspecifically bound
994 proteins. **C.** Immunoblot analysis of a reverse co-immunoprecipitation assay of the myc-tagged
995 TgABCE1 protein showing TgHCF101 is co-immunoprecipitating. The anti-SAG1 antibody was used as
996 a control for unspecifically bound proteins. **D.** TgHCF101 interacts with TgABCE1 in a Gal4-based yeast
997 two-hybrid assay. Co-transformed YRG2 cells expressing AD- and BD-fusion proteins were plated on a
998 control plate (+His, upper panel) for checking cell fitness and on the Y2H test plate (-His, mid panel),
999 and plates were incubated at 30°C. Yeast growth was recorder after 5 days. At the cell concentration
1000 used (OD_{600} =0.05), the observed interaction between AD-TgHCF101 and BD-TgABCE1 fusion proteins
1001 was strong enough to allow cell growth in the presence of 5 mM 3AT inhibitor (-his + 3AT lower panel).
1002 None of the proteins tested alone exhibited *HIS3* transactivation capacities. Results shown here are
1003 representative of three independent experiments. **E.** Immunoblot analysis of puromycin incorporation
1004 in the parental (TATi ΔKu80) and cKD TgHCF101 cell lines untreated or treated with ATc for 72h. TATi
1005 ΔKu80 treated with cycloheximide (CHX) was used as a control for translation inhibition. The
1006 puromycin signal was detected with anti-puromycin antibody, and total protein content was visualized
1007 by stain-Free imaging technology. Anti-actin antibody was also used as a loading control. **F.** Variation
1008 of puromycin incorporation in the different conditions was quantified by band densitometry and
1009 normalized on the total protein content of each respective lane. Puromycin labelling is presented as a
1010 percentage relative to the untreated control, set as 100% for each biological replicate. Values are
1011 represented as the mean and SD of 4 independent biological replicates; * p-value ≤ 0.05; ** p-value ≤
1012 0.01; ns, not significant (p-value ≥ 0.05), Student's *t*-test.
1013

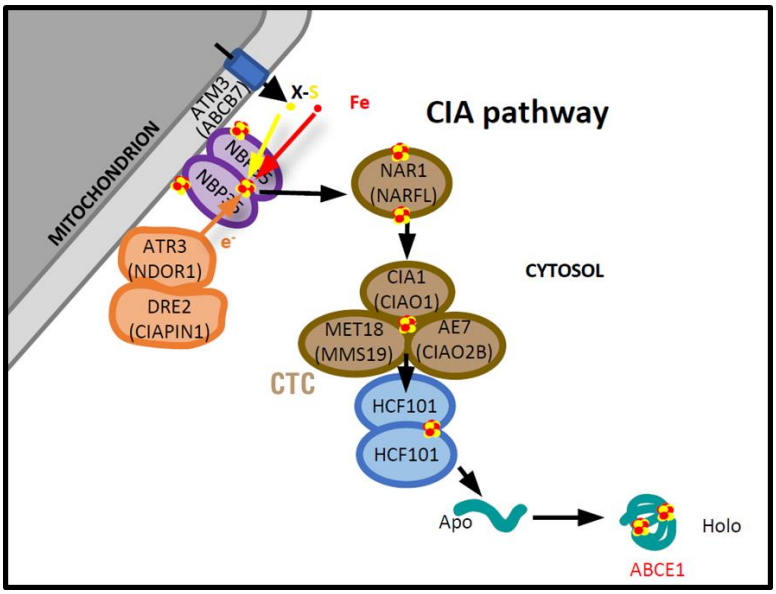

Figure 7. Schematic representation of the putative organization of the CIA pathway in *T. gondii.* This scheme places TgHCF101 as a Fe-S transfer protein from the CIA transfer complex (CTC) to client protein ABCE1. Plant nomenclature was used for the purpose of the figure, but names for human homologs are mentioned between brackets when appropriate.

1020 **Supplemental table legends**

1021 **Table S1.** Sequences used for the phylogenetic analysis displayed in Fig. 1A.

1022 **Table S2.** Proteins with higher expression upon depletion of TgHCF101 as found by label-free
1023 quantitative proteomics. For each protein candidate (with www.ToxoDB.org and www.Uniprot.org
1024 identifier), log_2 of the different ratio were calculated between the mean MaxQuant LFQ values found
1025 for the cKD HA-TgHCF101 mutant and the TATi ΔKu80 parental cell line. $-log_{10}$(pvalue) is also provided.
1026 Putative subcellular localization was obtained from the hyperLOPIT data available on ToxoDB.org, or
1027 by manual annotation. CRISPR fitness score and transcriptomic data for tachyzoites (Tz) and
1028 bradyzoites (Bz) were obtained from ToxoDB.org.

1029 **Table S3.** Proteins with lower expression upon depletion of TgHCF101 as found by label-free
1030 quantitative proteomics. For each protein candidate (with www.ToxoDB.org and www.Uniprot.org
1031 identifier), log_2 of the different ratio were calculated between the mean MaxQuant LFQ values found
1032 for the cKD HA-TgHCF101 mutant and the TATi ΔKu80 parental cell line. $-log_{10}$(pvalue) is also provided.
1033 Putative subcellular localization was obtained from the hyperLOPIT data available on ToxoDB.org, or
1034 by manual annotation. CRISPR fitness score and transcriptomic data for tachyzoites (Tz) and
1035 bradyzoites (Bz) were obtained from ToxoDB.org.

1036 **Table S4.** Proteins identified as co-immunoprecipitating with TgHCF101 through comparative mass
1037 spectrometry analysis of immunoprecipitated extracts form the cKD HA-TgHCF101 cell line frown or
1038 not in the presence of ATc.

1039 **Table S5.** Oligonucleotides used in this study.